Results in Chemistry 16 (2025) 102377

Contents lists available at ScienceDirect

Results in Chemistry

journal homepage: www.sciencedirect.com/journal/results-in-chemistry

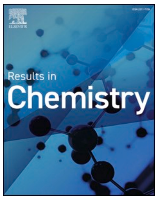

Fish scale-based carbon dots with g-C_3N_4 as a photo-catalyst for oxidation of herbicide 2,4-dichloro phenoxy acetic acid under visible light: Experimental and theoretical studies

Yessenia-Scarlette García-Gutierrez [a], Cristian-Brayan Palacios-Cabrera [a], Alan-Javier Santiago-Cuevas [a], Ivan-Alejandro Reyes-Domínguez [b], Maria-Teresa Orta-Ledesma [c], Frank Güell [d,e], Eduard Llobet [e], Edilso Reguera [f], Carlos Alberto Huerta-Aguilar [g,*], Pandiyan Thangarasu [a,*]

[a] Facultad de Química, Universidad Nacional Autónoma de México, Ciudad Universitaria, México City 04510, Mexico
[b] Instituto de Metalurgia, Universidad Autónoma de San Luis Potosí, San Luis Potosí 78210, San Luis Potosí, Mexico
[c] Instituto de Ingeniería, Universidad Nacional Autónoma de México, Ciudad Universitaria, Mexico City 04510, Mexico
[d] Facultat de Física, ENFOCAT, Universitat de Barcelona, 08028 Barcelona, Catalunya, Spain
[e] School of Engineering, MINOS, Universitat Rovira i Virgili, 43007 Tarragona, Catalunya, Spain
[f] Centro de Investigación en Ciencia Aplicada y Tecnología Avanzada, Instituto Politécnico Nacional, Unidad Legaria, Mexico City, Mexico
[g] School of Engineering and Sciences, Tecnologico de Monterrey, 72453 Puebla, Mexico

ARTICLE INFO

Keywords:
Fish scale-based carbon dots (NCDs@g-C_3N_4)
Photo-catalyst
G-C_3N_4 polymer
2,4-D herbicide and DFT

ABSTRACT

2,4-dichloro phenoxy acetic acid (2,4-D) has been employed as an herbicide to increase crop yields and ensure large-scale food production; however, it is highly toxic and persistent in the environment. This work deals with the green chemistry preparation of carbon quantum dots (NCDs) from fish scales and then combines them with graphitic carbon nitride to oxidize 2,4-D under visible light. The samples, C-NCDs, S-NCD, g-C_3N_4, C-NCD/g-C_3N_4, and S-NCD/g-C_3N_4 were characterized by different analytical methods (XRD, SEM, TEM, HRTEM, XPS, and fluorescence/UV–visible spectra). C-NCD/g-C_3N_4 and S-NCD/g-C_3N_4 are thermally stable, and the average size of the particles was ~5.0–15 nm. SEM/TEM show that quasi-spherical particles (7–20 nm) of C-CQD and S-NCD are homogeneously dispersed, and the fluorescence emission spectra show distinct profiles as C-NCDs (429 nm) and S-NCDs (318 nm and 404 nm), caused by hetero atoms from the fish scales that are less pronounced for C-NCDs. This is consistent with the photoluminescence spectra that C-NCDs and S-NCDs exhibit a green visible emission at 575 and 526 nm, respectively, as a typical behavior of carbon quantum dots. The bandgap energy of the samples (2.77–2.91 eV) is consistent with those from the Density Functional Theory (DFT). The adsorption of 2,4-D by S-NCDs/g-C_3N_4 is highly efficient; for example, $q_m = 2.85 \times 10^{-5}$ mol/g for C-NCD/g-C_3N_4, 2.02×10^{-5} mol/g for S-NCD/g-C_3N_4 or 2.43×10^{-5} mol/g for g-C_3N_4. The photocatalytic oxidation of 2,4-D by the samples reveals that there is considerable photocatalytic oxidation and follows first-order kinetics in the substrate as follows: $k_{visible} = 4.3 \times 10^{-3}$ mM s^{-1} and $k_{solar} = 7.5 \times 10^{-3}$ mM s^{-1} for C-NCDs/g-C_3N_4; $k_{visible} = 5.4 \times 10^{-3}$ mM s^{-1} and $k_{solar} = 10.4 \times 10^{-3}$ mM s^{-1} for S-NCDs/g-C_3N_4. In the cell images, although C-NCD and S-NCD exhibit dispersed fluorescence, adding C-NCD or S-NCD results in a significant fluorescence increase.

1. Introduction

Herbicides, namely, 2,4-D (2,4-dichloro phenoxy acetic acid), are essential in modern agriculture to increase crop yields and ensure large-scale food production. Their effectiveness and cost-efficiency make them valuable tools for farmers [1]. However, using 2,4-D in agriculture leaches into the environment, which is highly persistent (soil and water), causing environmental issues and disrupting aquatic ecosystems [2,3]. The presence of 2,4-D in water poses a potential risk to health and biodiversity [4], and a suitable-sustainable strategy for its remediation is imperative. Graphite carbon nitride (CN, g-C_3N_4), a polymer semi-conductor with a bandgap energy of 2.7 eV, exhibits blue intrinsic

---

* Corresponding authors.
E-mail addresses: huertaa@tec.mx (C.A. Huerta-Aguilar), pandiyan@unam.mx (P. Thangarasu).

https://doi.org/10.1016/j.rechem.2025.102377
Received 21 February 2025; Accepted 17 May 2025

photoluminescence at approximately 470 nm [5,6]. g-$C_3N_{4,}$ which has environmentally friendly, non-toxic, and stable features, is considered to be a valuable photocatalytic material [7–11]. The two-dimensional layered structure of g-C_3N_4, which is stabilized by van der Waals (vdW) forces present between the C—N layers, generates the structural framework, where carbon and nitrogen atoms have been bonded through the sp^2 hybridization, which gives high chemical stability similar to graphene's physicochemical properties [12]. Although g-C_3N_4 distinctive layered structure owns outstanding chemical stability, it exhibits several disadvantages that impact its photocatalytic properties, such as slow charge transfer, a low surface area of active sites, a narrow light absorption window, and a high recombination rate of electrons and holes [13–15]. So, several efforts have been made to modify the g-C_3N_4 structure to enhance the photocatalytic properties, including defect engineering, structural adjustment, and metal or non-metal doping [16]. Among these, the doping of non-metal heteroatoms such as S, P, B, and O with g-C_3N_4 has significantly impacted the catalytic properties [17–19]. The replacement of nitrogen by carbon in g-C_3N_4, while sulfur and iodine can substitute nitrogen in the triazine ring, can enhance the electrochemical, photophysical, and photochemical properties. The heterojunction of BiOBr with g-C_3N_4 has improved the photocatalytic activity, with a low electron recombination rate [20,21]. The photocatalytic performance of g-C_3N_4 can be finely tuned if its structure is suitably modified [22,23]. The incorporation of elements, such as boron [24,25], iodine [26], bromine [27], sulfur [15,23,28], and phosphorus [29] has effectively reduced the Eg of g-C_3N_4 and improved the optical absorption properties and it extends the lifetime of photogenerated electrons while shortening the electron transfer distance. Especially, sulfur-doped g-C_3N_4 has been attracting attention in the generation of a heterojunction structure, which inhibits the photo-generated charge recombination (i.e., spatial separation of e and h+). The isotype heterojunction possesses a greater advantage in charge separation than heterojunctions since the electronic structural properties are similar for compatibility [30]. Therefore, the fabrication of g-C_3N_4 combined with CQDs is essential and challenging. Sulfur doping, in particular, has been demonstrated to alter the electronic structure of g-C_3N_4, leading to enhanced conductivity. Another approach to enhance the electrochemical performance of g-C_3N_4 is to combine it with highly conductive materials. Since g-C_3N_4 possesses some electron migration capability, the overall electron transport efficiency of the composite can be significantly improved when combined with highly conductive materials [31,32]. The doping of S, P atoms could adjust the electronic and optical properties, especially by inserting these elements, which can either replace carbon or nitrogen in the g-C_3N_4 lattice or be placed directly into the structural layers. Thus, it can improve photocatalytic properties.

Carbon nitride can be synthesized through the direct thermal polymerization of melamine [33,34], dicyandiamide [35,36], and thiourea [37]. It consists of orderly sheets of tri-*s*-triazine moieties connected through planar tertiary amino groups, with C/N ratios of 0.75 or higher for g-C_3N_4. g-C_3N_4 is being widely considered in various fields, such as environmental remediation [38–41], energy conversion [33,42,43], photocatalytic H_2 production under visible light [44–48], photoelectrochemistry [49,50], photoluminescent [51–53], phototherapy [54,55], chemical/bio-sensing [56–59], bioimaging [60,61], and biomedicine [62–65]. In the molecular structure, the overlapping of N_{pz} and C_{pz} orbitals results in the formation of the highest occupied molecular orbital (HOMO) and the lowest unoccupied molecular orbital (LUMO), with respective band edges at +1.6 V (lower than $O_2/H_2O = 1.23$ V) and − 1.0 V (higher than $H^+/H_2 = 0$ V) (NHE) at pH = 7; therefore, g-C_3N_4 is thermodynamically suitable for water-splitting studies [66,67]. Another drawback of g-C_3N_4 lies in the large grain size of carbon nitrides, which results in a small specific surface area [68,69], limiting the charge carrier mobility that impacts the practical application of photocatalysts [70]. Furthermore, the low crystallinity of CN leads to lattice defects, which reduce the efficiency of photocatalysis by hindering the separation of photo-excited electron-hole pairs; [50–52] besides, the large size of CN can lead to a low photoluminescence quantum yield and poor water solubility, which also hinders its practical applications [71–75]. Increasing the crystallinity of CN can help reduce the recombination of charge carriers and improve the light-harvesting efficiency.

Carbon Dots (CDs) were discovered during the purification of single-wall carbon nanotubes [76–78]. Similar to the g-C_3N_4 structural and electronic properties, traditional quantum dots (QDs) exhibit photochemical properties and possess excellent biocompatibility, low toxicity, and minimal cell damage [79–83]. Consequently, they have wide-ranging applications in biosensors [84], due to their excellent light stability and resistance to photobleaching [85–87]. Doped CDs can contain elements such as nitrogen, oxygen, sulfur, and fluorine, and functional groups like —COOH, —NH_2, —OH, and —SH can be anchored on their surface. Among the synthetic methods (top-down or bottom-up), the bottom-up technique (utilizing hydrothermal and microwave methods), specifically the pyrolysis of molecular precursors, results in the production of small CDs with varying colors (yellow, orange, or brownish) depending on their size [88,89]. These CDs are spherically symmetrical, with a diameter of less than 10 nm, and can have either an amorphous or crystalline structure, exhibiting enhanced quantum yields. Amorphous and crystalline CDs possess intriguing properties, including photoluminescence and wavelength-dependent emission, high solubility, low toxicity, ease of functionalization, and biocompatibility [84]. Consequently, CDs have garnered significant attention from researchers due to their diverse technological applications in sensors, photocatalysis, bioimaging, drug delivery systems, solar cells, and LED devices [90]. Carbon quantum dots (NCDs) exhibit interesting photoactive properties, acting as photocatalysts for degrading organic pollutants [91] [92]; however, producing CDs through a chemical process is costly and generates unwanted/toxic intermediates as subproducts. Thus, it requires a green chemistry process [93].

In this context, the combination of g-C_3N_4 with quantum dots (QDs) can generate interesting photochemical and photophysical properties because of the synergic effect generated between the two components. The presence of heteroatoms, particularly sulfur and phosphorus, within the C-NCDs/g-C_3N_4, and S-NCDs/g-C_3N_4 plays a significant role in modifying the electronic properties of the g-C_3N_4 matrix. Sulfur atoms can introduce sub-energy levels (shallow donor levels) near the conduction band, enhancing the separation of photogenerated electron-hole pairs and facilitating electron transport. The phosphorus doping is known to introduce mid-gap states and can enhance the conductivity of the sample by narrowing the bandgap slightly. If high-energy photons excite the V_B electrons (vacancies in HOMO, considered as positive charged holes) to C_B level, i.e., from the highest occupied molecular orbital (HOMO) to the lowest unoccupied molecular orbital (LUMO), it results a charge separation generating the electron-hole pairs. The electrons in the LUMO involve in reduction reaction, and the holes in the HOMO participated in the oxidation reaction [22,94]. The delocalized π-conjugation in the structure can produce superoxide radicals ($\bullet O_2^-$) and hydroxyl radicals ($\bullet OH$) [5,6,95,96]. The modified g-C_3N_4 can be the ideal material for environmental remediation. Interestingly, we synthesized NCDs from biological waste fish scales, which are economically unexploited waste material, as green chemistry processes are growing from an environmental point of view [93]. NCDs are then combined with CDs to result in C—N, CDs/g-C_3N_4 and S-NCDs/g-C_3N_4 composites. Thereafter, the samples are employed as photocatalysts for the oxidation of 2,4-D. The results were compared to those obtained from C-NCDs, S-NCDs, g-C_3N_4, C-NCDs/g-C_3N_4, and S-NCDs/g-C_3N_4 (non-metal oxide photocatalysts). Furthermore, Density Functional Theory (DFT) was used to model the carbon nitride combined with carbon dots to understand their intrinsic properties. In particular, g-C_3N_4, NCD, and C-NCDs/g-C_3N_4 have been modeled and optimized through HSEh1PBE/LANL2DZ to understand the geometrical and electronic properties.

2. Material and methods

2.1. Materials

All reagents were purchased from Sigma-Aldrich and used without any further purification. Melamine ($C_3H_6N_6$), citric acid ($C_6H_8O_7$), and urea (NH_2CONH_2) were obtained from Sigma Aldrich. Fish scales were acquired from a local market in Mexico City. 2,4-Dichlorophenoxyacetic acid organochlorine herbicide was obtained from the plant media world.

2.2. Synthesis

g-C_3N_4: The pure graphitic carbon nitride (g-C_3N_4) was synthesized using a fractional thermal polymerization method (pyrolysis). Melamine (2.0 g) was placed in a ceramic crucible and subjected to ramp calcination. Initially, it underwent a thermal treatment at 320 °C for one hour, followed by a temperature increase to 500 °C for three hours at a heating rate of 10 °C/min. The resulting product was then characterized by different analytical techniques and then used in combination with carbon dots.

Conventional carbon dots (C-NCDs): Carbon quantum dots were prepared using conventional methodology. In a standard procedure, citric acid (3.0 g) and urea (1.0 g) in a 3:1 ratio were dissolved in a Teflon beaker with 25 mL of deionized water. The mixture was then transferred to an autoclave reactor and maintained at 180 °C for 12 h. Subsequently, the brown liquid obtained was then filtered three times using a 2.0 μm filter paper.

Sustainable carbon dots (S-NCDs)*:* Sustainable carbon dots are synthesized from fish scales obtained from a local food market. These scales were washed several times to remove residue, dried at 60 °C, and ground. 1.5 g of the resulting powder was added to an autoclave and heated at 200 °C for 12 h. The brown liquid obtained was then filtered three times using 2.0 μm filter paper.

NCDs/g-C_3N_4 and S-NCDs/g-C_3N_4: The NCDs/g-C_3N_4 and S-NCDs/g-C_3N_4 composites were prepared by impregnating NCDs onto g-C_3N_4 in a 1:1 ratio under magnetic stirring for 2 h. Briefly, NCDs/g were dissolved in deionized water (30 mL), to which g-C_3N_4 NPs (1.2 g) were added under sonication and agitated for 30 min. The obtained mixture was transferred into a Teflon-containing autoclave and then heated (180C) for 24 h. After cooling, the isolated sample was dried in an oven for 3 h before the characterization. The same procedure was adopted to obtain S-NCDs/g-C_3N_4 after considering S-NCDs (1.2 g, mM) /g-C_3N_4 (0.3 g).

Scheme 1 shows synthesis process.

2.3. Characterization details

The crystallinity of the samples was evaluated using powder X-ray diffraction (XRD) on a Rigaku RU300 diffractometer and Cu Kα radiation (wavelength $\lambda = 0.154$ nm). The obtained data were compared with the American Mineralogist Crystal Structure Database (AMCSD) to identify the crystalline planes. The particles' average size and the crystal lattices' average length were determined using Scherrer's formula. The samples were further characterized by Fourier transform Infrared spectra (FT-IR, Perkin Elmer RR instrument) focusing on C—C, C═C, C—N, and C═N bonds. Scanning electron microscopy (SEM) was performed using a Quanta 600 Environmental Scanning Electron Microscope (ESEM) with X-ray microanalysis to analyze the morphology of the samples. The composition of elements was estimated by Energy Dispersive X-ray spectrometry (EDS, micro analyzer resolution 61.0 eV), employing the Cliff-Lorimer Ratio Thin Section quantitative method with Silicon (K series) as standard. The samples' morphology and crystallinity (C-NCDs, S-NCDs, g-C_3N_4, C-NCDs/g-C_3N_4, and S-NCDs/g-C_3N_4) were further analyzed by a Transmission Electron Microscope (TEM, JEOL 2010, 200 kV) equipped with a LaB6 thermo ionic cannon (40 kV acceleration). For the samples, high-resolution transmission electron microscopy (HRTEM) was also performed on a JEOL 1011 at 200 kV to analyze the structure. UV–visible absorption of the samples was measured on the Perkin Elmer Lambda 25 instrument, and the solid-state diffuse reflectance was performed on a Perkin Elmer Lambda 2 instrument; furthermore, the fluorescence properties of the samples in solution were studied by using the F96Pro instrument, and the photoluminescence was measured at room temperature using a chopped Kimmon IK Series He—Cd laser (325 nm and 40 mW) with a filter of 360 nm that was used against stray light. All spectra were corrected for the response function of the setups. The luminescence was dispersed with an Oriel Corner Stone 1/874000 monochromator, detected using a Hamamatsu H8259–02 with a socket assembly E717–500 photomultiplier, and amplified through a Stanford Research Systems SR830 DSP.

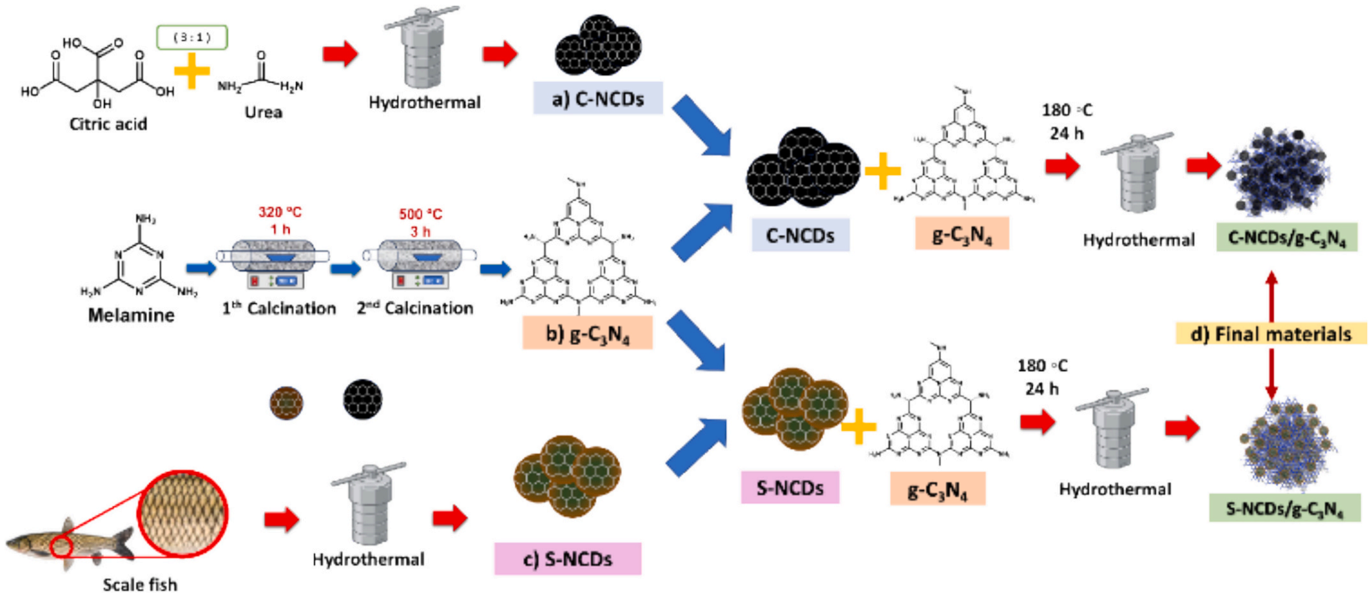

Scheme 1. Synthesis: a) C-NCDs, b) C-NCDs, c) g-C_3N_4, and d) NCDs/ g-C_3N_4.

2.4. 2,4-D degradation

The degradation of 2,4-dichlorophenoxyacetic acid was studied under visible light (100 W LED) and also under solar irradiation with an intensity of 50,000 lm per square meter (lux). The photocatalytic efficiency of g-C_3N_4, C-NCDs, S-NCDs, C-NCDs/g-C_3N_4, and S-NCDs/g-C_3N_4 was analyzed by using 2,4-dichlorophenoxyacetic acid (2,4-D) (Scheme 2) under visible and solar irradiation. An aqueous solution of 2,4-D (5.0 mg/L) containing NCDs/g-C_3N_4 or S-NCDs/g-C_3N_4 (0.5 g) was exposed to visible light (200 W) over 3 h, and the concentration of 2,4-D was measured every 20 min by UV–Vis absorption spectroscopy (Lambda 25) at 280 nm. (See Scheme 3.)

2.5. Computational details

Computational method Density Functional Theory (DFT) allows the modeling of semiconductors in order to understand their intrinsic properties and foresee their potential application even before their production in the lab. Joint experimental and computational studies can save time and resources in developing new-generation semiconductors applied to pollutant degradation. g-C_3N_4 was constructed using a 340-atom monolayer model with a formula $(C_3N_4)_{46}H_{19}$. For NCDs, a 204-atom supramolecule resulting from the amide condensation of citric acid and urea in a 3:1 stoichiometric ratio was modeled with a formula $(C_{10}H_{12}O_{10}N)_6$. The composite material was thus a 1:1 NCDs/ g-C_3N_4 system composed of 544 atoms and with a formula $C_{201}H_{93}O_{61}N_{189}$. Each of these molecules was optimized using the HSEh1PBE functional and a LANL2DZ basis set. For all cases, a Polarizable continuum model (PCM) was utilized, considering water as the solvent at 298 K and 1 bar.

3. Results and discussion

3.1. XRD studies

The XRD diffraction patterns of samples such as C-NCDs, S-NCDs, g-C_3N_4, C-NCDs/g-C_3N_4, and S-NCDs/g-C_3N_4 were recorded (Fig. 1) and observed the characteristic peaks of C-NCDs and S-NCDs at angles of 18.70° and 21.87°, respectively, corresponding to disordered carbon atoms (002). [97] The difference in angle is due to the presence of minerals in the S-NCDs originating from fish scales. Pure-phase g-C_3N_4 displays the characteristic peaks at diffraction angles of 13.05° for the crystal plane (100) and 27.33° for the plane (002). [98,99] In the composite materials C-NCDs/g-C_3N_4 and S-NCDs/g-C_3N_4, the crystal planes (002,100) for g-C_3N_4 planes exhibit a greater intensity than that observed for the NCDs.

3.2. TGA studies

The thermal stability (50 to 900 °C) of melamine, C-NCDs, S-NCDs, g-C_3N_4, C-NCDs/g-C_3N_4, and C-NCDs/g-C_3N_4 samples was studied through TGA analysis (Fig. 2). In Fig. 2a, the TGA curve for melamine reveals a distinct weight loss at approximately 350 °C, signifying complete thermal degradation of melamine into volatile products. The TGA estimates the total weight loss (98.17 %) of g-C_3N_4 at 900 °C, while for C-NCDs/g-C_3N_4 and S-NCDs/g-C_3N_4, total weight loss of 99.99 % at the same temperature, attributed to the carbon dots decomposition, and it means that the weight loss difference (~1.82 %) is associated with the carbon dots composited into the g-C_3N_4 matrix. So, the estimated weight ratio of NCDs to g-C_3N_4 was approximately 1:54. For C-NCDs (Fig. 2b), the weight loss occurs in two primary stages: the first at around 150 °C, representing 3.52 % of the weight, which is likely attributed to the loss of surface-bound water or volatile organic groups, and in the second, a notable weight loss of 50.52 % between 200 °C and 600 °C attributes to the degradation of carbon-based structures. At 800 °C, the residual mass is about 31.08 %, indicating the material's stability at higher temperatures. The TGA profile for S-NCDs (Fig. 2c) displays a similar multi-step degradation pattern, observing an initial weight loss of 2.57 % (~150 °C) attributed to the loss of adsorbed water or surface groups. The primary decomposition occurs between 200 °C and 600°, resulting in a significant weight loss of 27.39 % due to the decomposition of the functional groups such as carboxylic groups (—COOH), carbonyls (C=O) and other surface oxygenated groups, followed by a smaller weight loss at 700 °C caused by the breaking of stable C—O—N bonds. [100] The final residue at 800 °C is 3.08 %, indicating comparatively lower thermal stability than C-NCDs. The g-C_3N_4 sample (Fig. 2d) demonstrates high thermal stability, with only 1.83 % weight loss observed below 400 °C, likely due to the release of trapped gases or adsorbed moisture. A significant weight loss of 98.17 % is noticed above 600 °C, corresponding to the thermal decomposition of the g-C_3N_4 framework.

The composite C-NCDs/g-C_3N_4 (Fig. 2e) exhibits a more intricate degradation pattern. Initially, there is a minor weight loss (2.62 %) around 150 °C, followed by a larger decomposition step between 300 °C and 600 °C, which accounts for 4.59 % of the weight. The thermal stability (92.79 %) is noted at 800 °C, indicating that the integration of C-NCDs with g-C_3N_4 enhances the stability of the composite compared to pure C-NCDs. A similar observation was seen for S-NCDs/g-C_3N_4 (Fig. 2f), showing improved thermal stability compared to S-NCDs alone. The first weight loss (1.54 %) occurs below 200 °C; a major weight loss of 3.77 % is observed between 300 °C and 600 °C. The stability of the composite mass at 800 °C is 94.69 %, suggesting the presence of a stable g-C_3N_4. This means that both C-NCDs and S-NCDs undergo significant decomposition at intermediate temperatures, with S-NCDs exhibiting slightly lower thermal stability. Notably, if g-C_3N_4 is

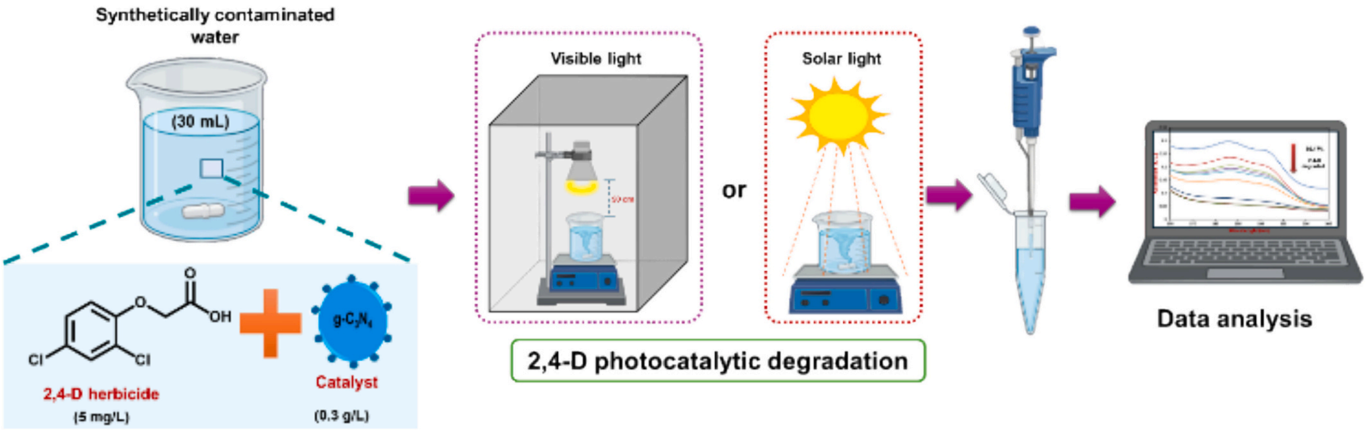

Scheme 2. The oxidation of 2,4-Dichlorophenoxyacetic acid under visible and solar lights.

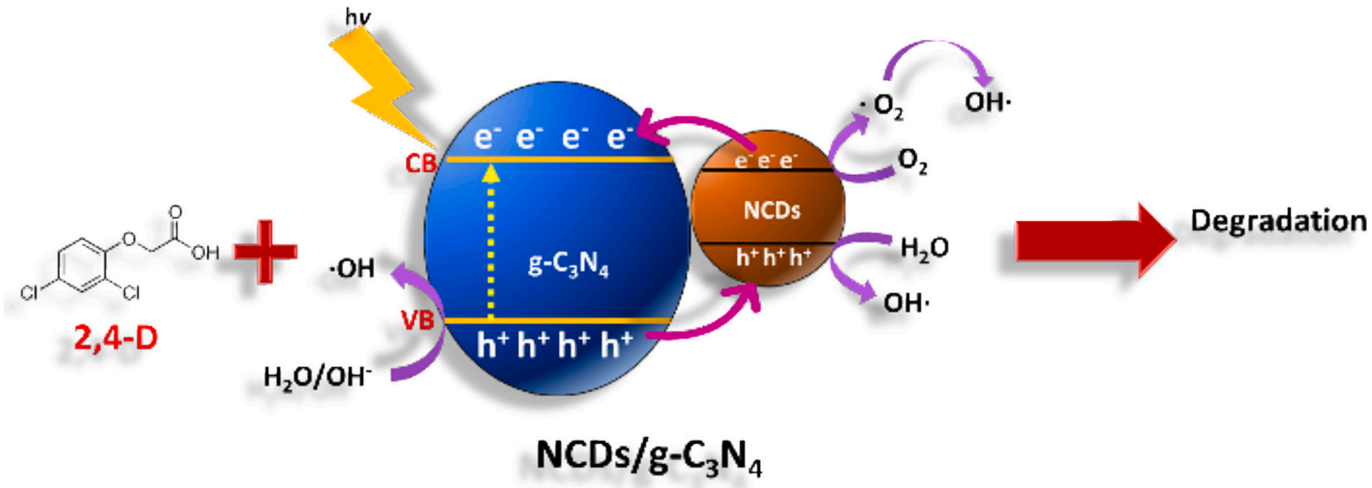

Scheme 3. Photocatalytic degradation of 2,4-dichloro phenoxy acetic acid by photocatalyst based on carbon dots from fish scale under visible light.

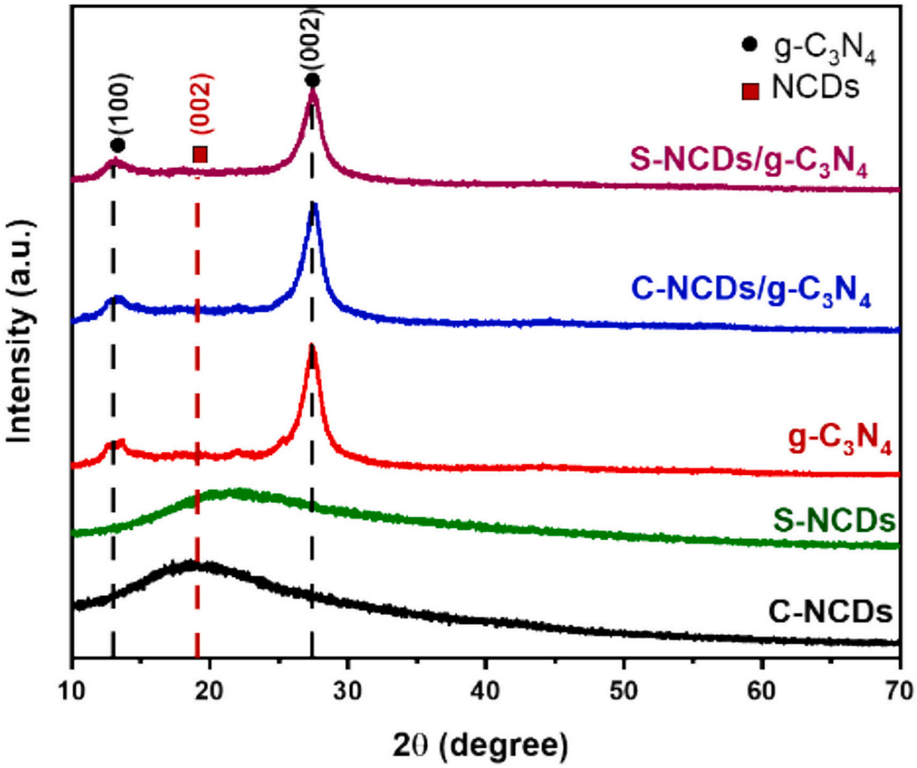

Fig. 1. XRD pattern of C-NCDs, S-NCDs, g-C_3N_4, C-NCDs/ g-C_3N_4, and S-NCDs/ g-C_3N_4.

incorporated into the NCDs, it significantly enhances the thermal stability of the resulting composites (g-C_3N_4 NCDs). [101]

3.3. XPS studies

X-ray photoelectron spectroscopy (XPS) was performed for C-NCD/g-C_3N_4 and S-NCD/g-C_3N_4, and the results show the signals corresponding to carbon, nitrogen, and oxygen. It is consistent with the composition of g-C_3N_4 and the surface functionalization of the incorporated NCDs (Fig. 3), agreeing with reported studies [102,103]. For S-NCD/g-C_3N_4 (derived from fish scales), the C 1 s peak was detected at 288 eV, attributed to N—C═N bonds presenting in the heptazine-based framework of g-C_3N_4, where carbonyl or carboxylic groups (C═O or COOH) are anchored on the surface of NCDs. The signal corresponding to N 1 s is observed at 399 eV as nitrogen species commonly found in g-C_3N_4 structure, such as C—N═C / C—NH—C) and N—$(C)_3$ units formed during the polycondensation process. The peak O 1 s was detected at 532 eV, indicating the presence of an oxygen-containing surface having hydroxyl (—OH), carbonyl, and ether functionalities, which are typically from carbonaceous biomass or partially carbonized under mild thermal conditions. Additionally, there were additional signals (975, 1106, and 1224 eV) in the higher binding energy region, and they may correspond to Auger transitions of carbon or to residual inorganic elements, especially calcium or phosphorus, which commonly exist in fish scales. So, the existence of these signals suggests that there is a more complex surface composition having trace minerals in the structure that may affect the material's surface reactivity. In the case of C-NCD/g-C_3N_4, similarly, the C 1 s (288 eV) and N 1 s (399 eV) were detected,

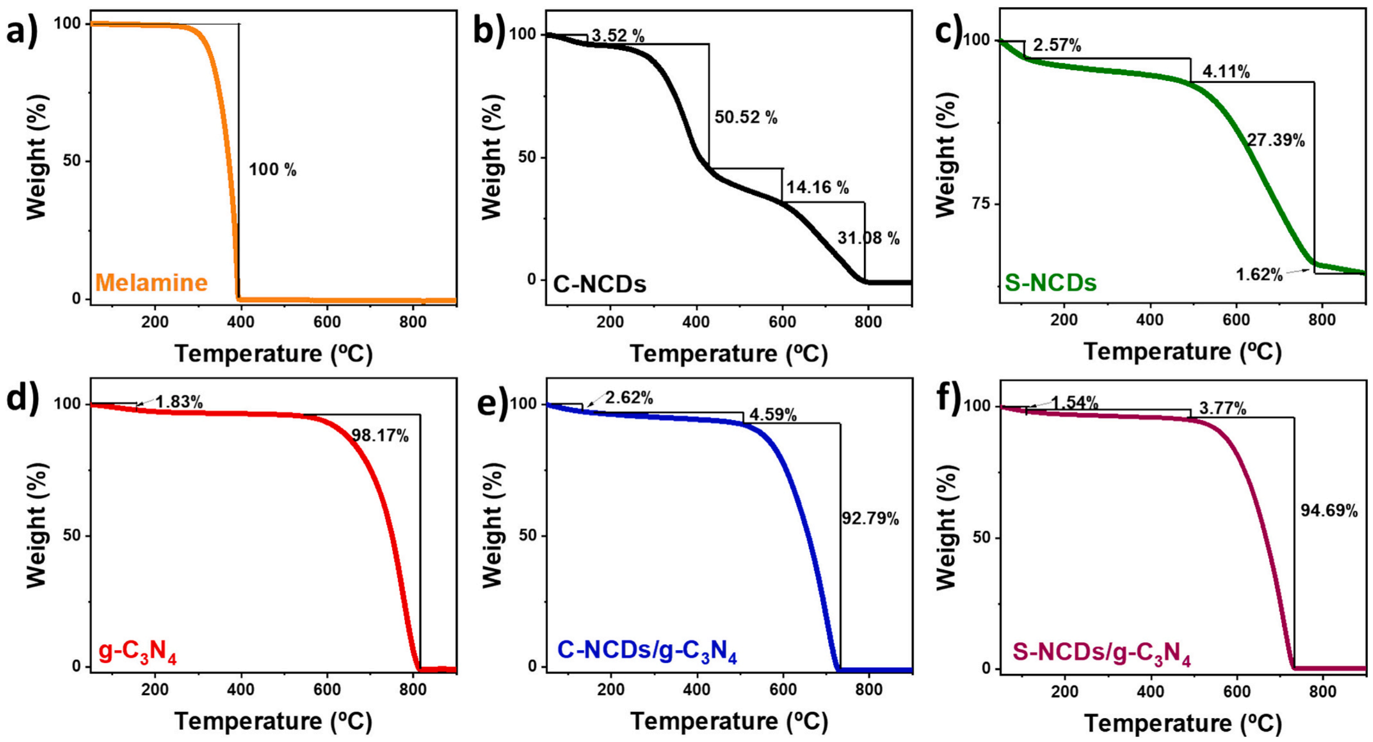

Fig. 2. TGA: a) melamine, b) C-NCD, c) S-NCD, d) g-C_3N_4, e) C-NCD/g-C_3N_4 and f) S-NCD/ g-C_3N_4.

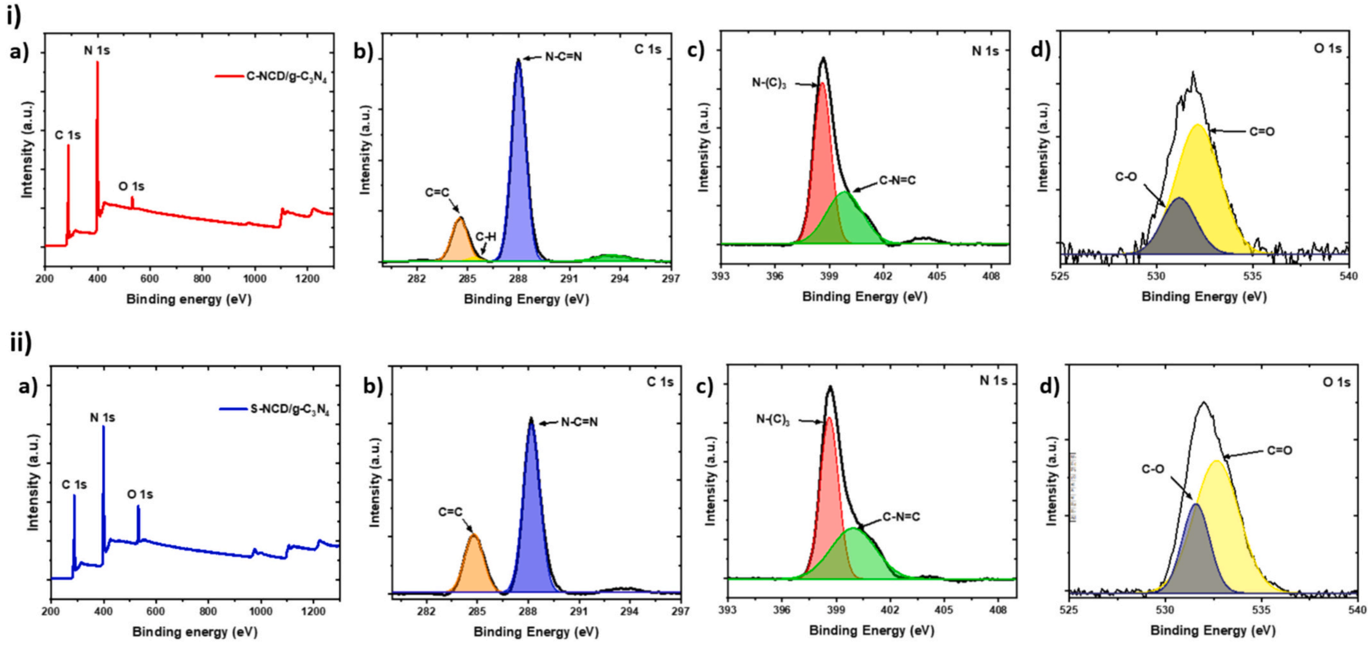

Fig. 3. XPS: **i)** C-NCD/g-C_3N_4 and **ii)** S-NCD/g-C_3N_4.

originating from the g-C_3N_4 backbone. The results are in agreement with the published work [103]. A strong appearance of the O 1 s peak at 532 eV can be attributed to the higher content of oxygenated groups in the NCDs derived from citric acid or carboxylic acids. Importantly, no signals attributable to inorganic elements such as calcium or phosphorus were observed; this indicates that there is a more uniform and free from other elements except C, N, and O, coinciding with controlled synthesis conditions [104]. For C-NCD/g-C_3N_4 and S-NCD/g-C_3N_4, there is a significant difference that can influence the physicochemical behavior, such as photocatalytic activity, surface charge dynamics, and interaction with environmental pollutants. Overall, the XPS results confirm not only the successful integration of NCDs into the g-C_3N_4 framework but also provide insight into how the electronic structure governs and the potential reactivity of the samples.

3.4. FT-IR studies

The FT-IR spectra of g-C_3N_4 and C-NCD (Fig. 4) display signals ranging from 3200 to 3000 cm^{-1}, potentially associated with N—H or O—H bonds (amines or hydroxyls). For g-C_3N_4, faint signals are detected

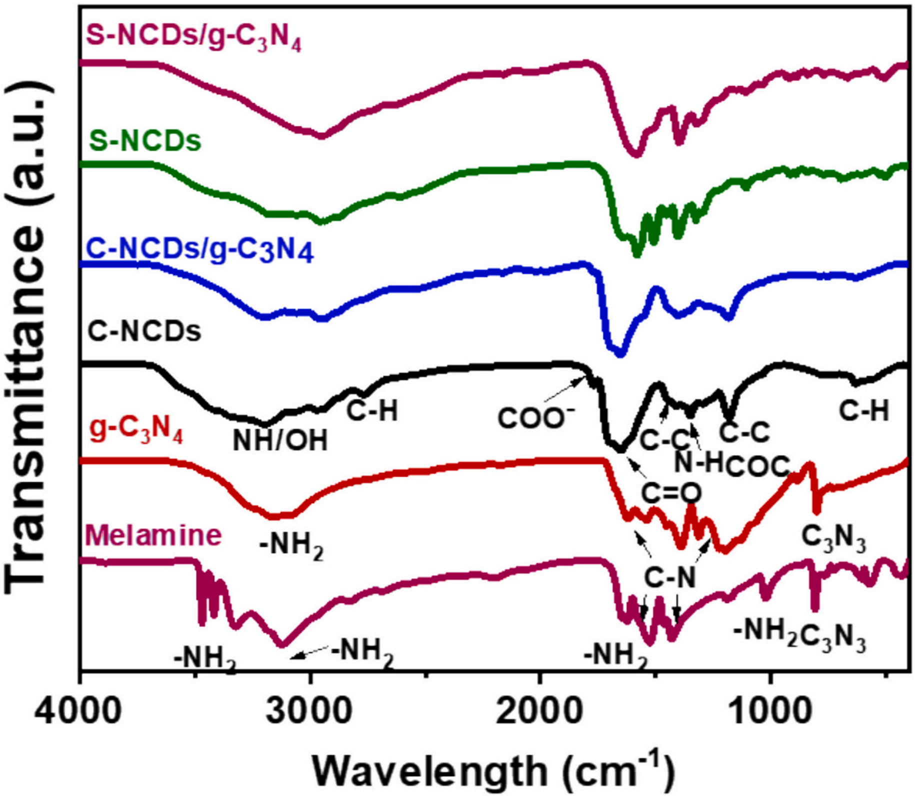

Fig. 4. FT-IR of melamine, g-C_3N_4, C-NCD, C-NCD/g-C_3N_4, S-NCD and S-NCD/g-C_3N_4.

at 573.12 cm^{-1} and 432.4 cm^{-1}, which may correspond to the vibrations of melamine molecules. The peaks at 807.11 cm^{-1} and 1028.45 cm^{-1} could be linked to the vibration of triazine rings. C-NCDs or S-NCDs exhibit 2957–2972 and 2763–2885 cm^{-1} peaks, corresponding to C—H bonds from alkyl groups (CH_2, CH_3). Additionally, the peaks at 1768, 1705, and 1650 cm^{-1} are associated with C═O stretching, potentially from carboxylic acids or esters, while the peaks at 1402–1417 and 1324–1353 cm^{-1} are related to in-plane C—H bending vibrations, likely from alkyl groups. The peak at 1646 cm^{-1} corresponds to C═O stretching of amides or carbonyl groups, and the peaks at 1575 and 1508 cm^{-1} correspond to C═C or C═N vibrations, indicating the presence of aromatic or amide bonds. The 1106–1187 and 631–698 cm^{-1} peaks correspond to C—O and C—H stretching, respectively. S-NCDs show peaks at 2972 and 2885 cm^{-1}, assigning to C—H bonds, while the peaks at 2616–2522 cm^{-1} are likely due to S—H bond vibrations (thiols). The characteristic of aromatic rings or C═C bonds and the peak at 503 cm^{-1} may be due to C—S or C-X (halogen) bond stretching vibrations. [92,105,106] The peak at 1673 cm^{-1} is associated with the C═O stretching of amides or conjugated carbonyls, possibly from g-C_3N_4, while the peaks (1562–1572 cm^{-1} and 1440–1510 cm^{-1}) have been assigned to C═C or C═N vibrations, related to aromatic structures or g-C_3N_4 bonds. The peak around 1035–1182 cm^{-1} is associated with C—O or C—N stretching, potentially originating from ethers or amines. Besides, the peaks at 2159 and 2012 cm^{-1} indicate the presence of C≡C or C≡N stretching in the samples, implying the presence of alkynes or nitriles. Finally, the peak at 636 cm^{-1} corresponds to out-of-plane C—H or C═O vibrations, typical of carbonyl or aromatic groups. [107,108]

Lastly, the 676 and 508 cm^{-1} peaks are attributed to C—S vibrations or in-plane C═C bending, commonly found in heterocyclic or aromatic structures. [92,106,108] On the other hand, the S-NCDs and S-NCDs/ g-C_3N_4 display additional groups, such as S—H, suggesting the presence of sulfur or phosphorus compounds, exhibiting additional features of more intricate structural modifications (such as C≡C or C≡N bonds).

3.5. SEM studies

SEM images were captured for g-C_3N_4, C-NCDs, and S-NCDs, showing that C-NCDs (x2300) produced from ethylenediamine and urea have demonstrated an irregular morphology and a uniform size distribution, with noticeable signs of agglomeration (Fig. 5, S1 and S2). S-NCDs (x8500), obtained from fish scales (Fig. 5c), have exhibited particles with more pronounced agglomeration, some slightly larger than others. Their rough surfaces reveal numerous filamentous structures and smaller particles. Lastly, the image of g-C_3N_4 (x15000), derived from melamine (Fig. 5a), displays a highly porous, agglomerated structure with rough edges, forming an interconnected network with numerous voids. The chemical composition of C-NCDs, S-NCDs, and g-C_3N_4 was analyzed using the EDS analysis (Table 1). All the samples contain carbon, nitrogen, and oxygen as common components. For S-NCDs, additional elements such as Na, K, S, and P were presented because the sample was prepared from fish scales, where sulfur and phosphorus are expected to be present.

3.6. HRTEM studies

The size and morphology of C-NCD, S-NCD, and g-C_3N_4 were analyzed using HRTEM (Fig. 5(ii)). C-CQD (Fig. 5d) exhibited uniform dispersion of particles, suggesting its amorphous nature due to the lack of clear crystalline structures. In contrast, S-NCD (Fig. 5e), derived from fish scales, displayed larger quasi-spherical particles ranging from 7 to 20 nm in size, with homogeneous dispersion. However, the high-resolution TEM image observed no particles with well-resolved lattice fringes. Finally, g-C_3N_4 showed a larger size, between 100 and 300 nm, with an irregular structure and uneven surface (Fig. 5f).

3.7. UV–visible spectra

The UV–Vis absorption spectra of the C-NCDs and S-NCDs exhibit

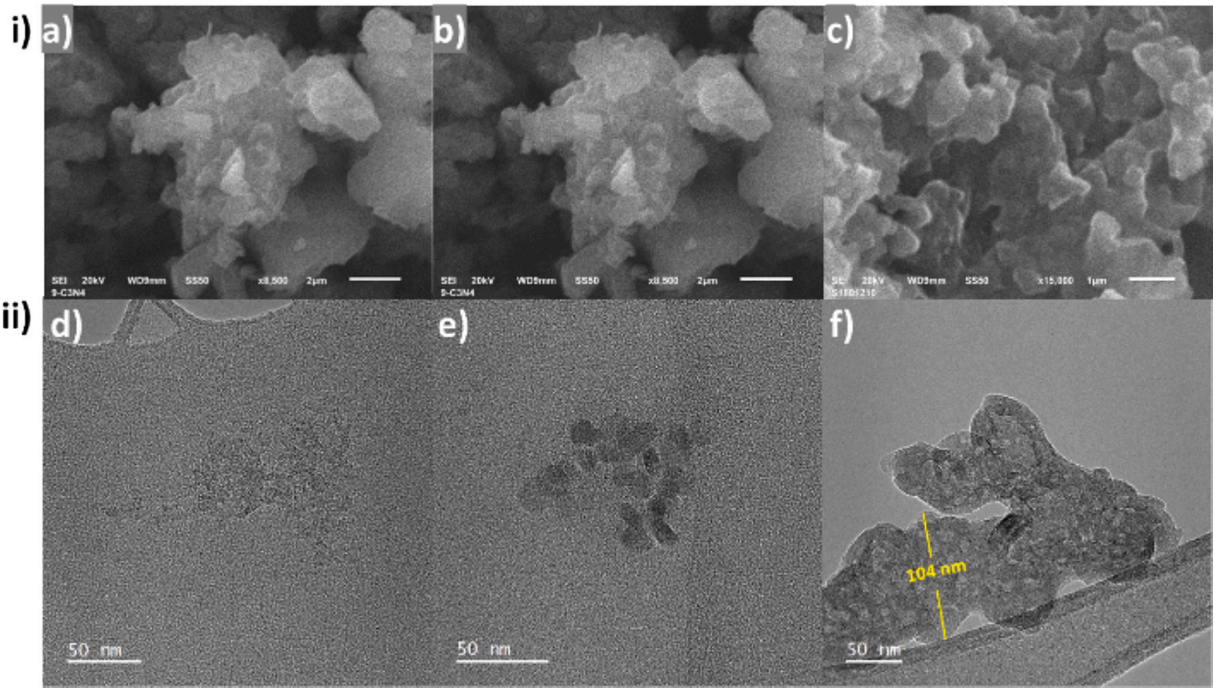

Fig. 5. (i) SEM images: a) C-NCD, b) S-NCD, and c) g-C_3N_4. **(ii)**. HRTEM: d) C-NCD; e) S-NCD; and f) g-C_3N_4.

Table 1
EDS elemental composition of the samples.

Sample	Elemental composition (Wt%)							
	N	C	O	Na	K	S	P	Ref.
C-NCDs	4.0	74.1	21.9	–	–	–	–	This work
S-NCDs	10.5	71.0	14.9	1.5	0.5	0.5	0.5	
g-C_3N_4	53.5	39.3	7.2	–	–	–	–	
g-C_3N_4	62.3	32.7	5.0	–	–	–	–	[109]
g-C_3N_4	58.95	41.05	–	–	–	–	–	[110]
UCQDs	17.2	59.9	22.9	–	–	–	–	[111]
CQD@LEU	46.4	40.5	1.6	–	–	–	–	[112]
CQDs	45.5	1.2	53.3	–	–	–	–	[113]

distinct electronic transitions, providing insight into their structural and electronic properties (Fig. 6a). While both types of carbon dots undergo similar n-π* transitions, the primary differences lie in the extent of conjugation and surface chemistry, with the fish scale-derived carbon dots demonstrating broader electronic delocalization and potentially more complex surface chemistry, leading to the observed redshift and higher absorption intensity. For example, C-NCDs demonstrate a maximum absorption peak at 334 nm, attributed to n-π* transitions of conjugated carbon systems, likely involving sp^2 hybridized carbon structures. [114] This peak suggests NCDs have relatively smaller aromatic domains or less extensive conjugation. In contrast, S-NCDs show a red-shifted absorption peak at 366 nm, corresponding to n-π* transitions. The redshift indicates a more extended conjugated system, possibly due to larger graphitic domains or increased functionalization on the surface, enhancing electron delocalization. [115] This increased conjugation may result from the organic matrix of the fish scales, introducing additional heteroatoms or oxygen-containing groups during synthesis, thereby affecting the electronic properties of the NCDs. Thus, S-NCDs exhibit notably higher absorption intensity, possibly reflecting greater absorptive centers or enhanced interaction between incident light and the material. This could arise from a higher density of surface functional groups facilitating electronic transitions or a larger particle size resulting in stronger light absorption.

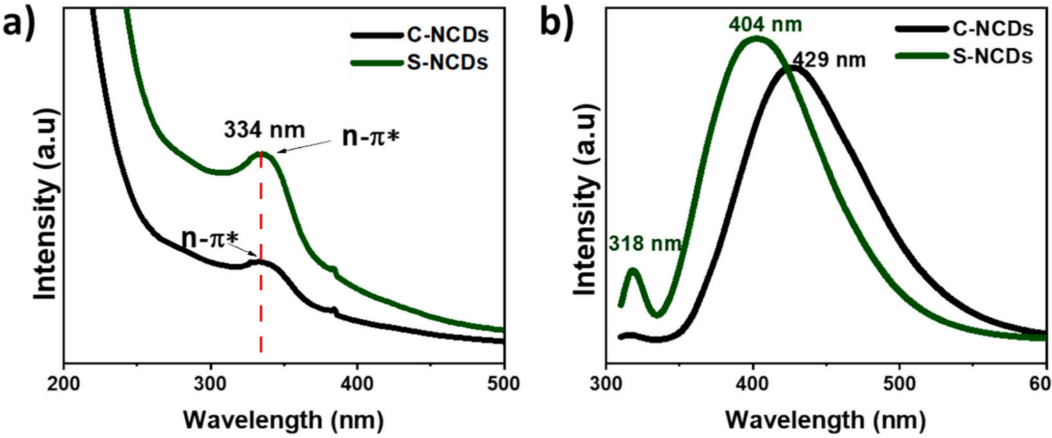

Fig. 6. a) UV–Vis spectra of C-NCDs and S-NCDs; b) Fluorescence of C-NCDs and S-NCDs

3.8. Fluorescence studies

The fluorescence spectra of C-NCDs and S-NCDs suspended in an aqueous solution (0.1 mM) show distinct differences in their emission profiles, which can be attributed to variations in their electronic structure, surface functional groups, and particle size (see Fig. 6b). C-NCDs exhibit a single, prominent emission peak at 429 nm when excited at (310 nm). This emission is a characteristic feature of carbon dots, where the photoluminescence is often influenced by surface defects, functional groups, or n-π* transitions within the conjugated domains. The relatively long emission wavelength suggests moderate conjugation and electron delocalization, with photogenerated electrons relaxing from higher energy states to emit in the visible range. [116] Conversely, S-NCDs demonstrate a more intricate emission pattern, displaying two distinct peaks: a faint one at 318 nm and a more intense peak at 404 nm and the former peak (318 nm) is situated in the near-UV spectrum, implying the existence of additional electronic transitions that are less pronounced for C-NCDs; this could be attributed to specific surface functional groups, likely from the organic material found in the fish scales for the introduction of new energy levels. The smaller peak (318 nm) could be attributed to the presence of smaller/less conjugated particles. In comparison, the larger peak at 404 nm likely represents most of the population, exhibiting slightly different electronic properties from conventionally synthesized dots [117]; moreover, the peak (404 nm) is blue-shifted somewhat compared to the C-NCDs, suggesting that the electronic structure of the carbon dots derived from fish scales leads to a slightly different relaxation pathway for photogenerated electrons. This blue shift may be attributed to smaller particle sizes or different surface chemistry, resulting in more confined electron states caused by a less extensive conjugation. Dual emission peaks in S-NCDs may also indicate heterogeneity in particle size or multiple emissive centers. Overall, although both carbon dots display fluorescence from similar mechanisms (surface defects, functional groups, and n-π* transitions), the fish scale-derived dots exhibit a more complex emission profile, likely due to the introduction of additional surface states and variations in particle size.

The fluorescence emission of C-NCDs/g-C_3N_4 and S-NCDs/g-$C_3N_3N_4$ (0.5 g/L) in an aqueous suspension (Fig. 7a) was recorded at 310 nm excitation, and the former sample exhibited an emission peak at 435 nm, while the latter emitted at 437 nm. In addition, the photoluminescent stability of both samples was analyzed by measuring the fluorescence intensity. The data were plotted against time and used to determine the photostability study (Eq. 1), as it is associated with the structural characteristics [118].

$$I(t) = I_0 \bullet e^{-t/\tau} \tag{1}$$

I(t) = fluorescence intensity over time, I_0 = initial intensity, t = time expressed in seconds, and τ = decay time constant. The τ values of 3340.62 s and 1681.58 s are obtained for S-NCDs/g-$C_3N_3N_4$, and C-NCDs/g-$C_3N_3N_4$, respectively. The half-life time was calculated using the equation $t_{1/2} = \tau\text{-}\ln(2) \approx 0.693\text{-}\tau$, obtaining $t_{1/2}$ values of 2315.08 s for S-NCDs/g-C_3N_4 and 1165.33 s for C-NCDs/g-C_3N_4, showing that the former exhibits a decay time constant approximately twice that of the latter. This greater resistance for S-NCDs/g-$C_3N_3N_4$ may be attributed to the incorporation of sulfur atoms in its structure that could facilitate forming additional bands near C_B, and it can reduce the overall bandgap energy [119].

3.9. Solid-state reflectance spectra

The UV–Vis solid reflectance spectra were recorded for C-NCDs/g-C_3N_4, S-NCDs/g-C_3N_4, and g-C_3N_4, and the direct and indirect bandgap energy (E_g) was calculated by extrapolating to the X-axis in the Tauc plot using eqs. (2) and (3):

$$(\alpha h\nu)^n = \mathrm{K}\left(h\nu - E_g\right) \tag{2}$$

$$(\alpha h\nu)^{1/n} = \mathrm{K}\left(h\nu - E_g\right) \tag{3}$$

$h\nu$ = energy of the incident photon, α = absorption coefficient, K = energy constant, and n = nature of the transition, with $n = 2$. The E_g value is presented in eV.

The Tauc method's bandgap analysis (Fig. 8 (i)) revealed no significant variations among the samples; for example, g-C_3N_4 demonstrated a direct bandgap of 2.89 eV and an indirect bandgap of 2.77 eV, indicating easier electronic transitions in the indirect case. C-NCDs/g-C_3N_4 exhibited values of 2.91 eV and 2.81 eV for the direct and indirect gaps, respectively, suggesting improved indirect electron transitions. S-NCDs/g-C_3N_4 displayed a direct bandgap of 2.93 eV and an indirect bandgap of 2.78 eV, implying a greater ease for indirect transitions. These findings suggest that the electronic properties of g-C_3N_4 are modified by doping with carbon dots from different sources, impacting both the direct and indirect bandgaps.

3.10. Photoluminescence (PL) analysis

The PL spectra were obtained at room temperature with UV excitation at 325 nm (Fig. 8 (ii)) and shows that the S-NCDs have displayed the

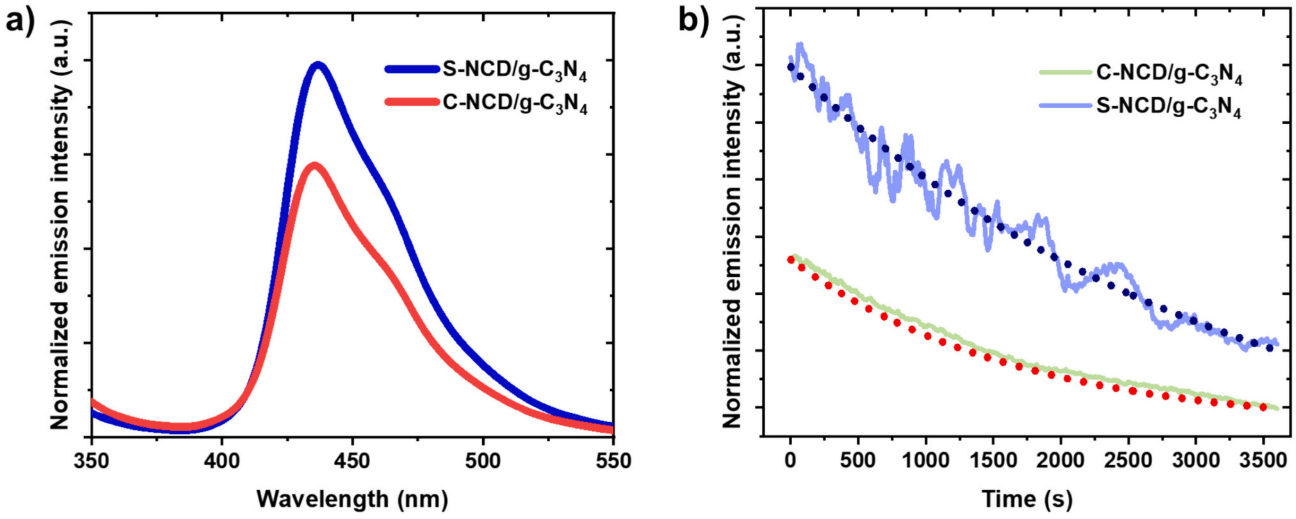

Fig. 7. a) Fluorescence of C-NCDs/g-C_3N_4, S-NCDs/g-C_3N_4 and b) Long-scale time-resolved fluorescence analysis of C-NCDs/g-C_3N_4, S-NCDs/g-C_3N_4.

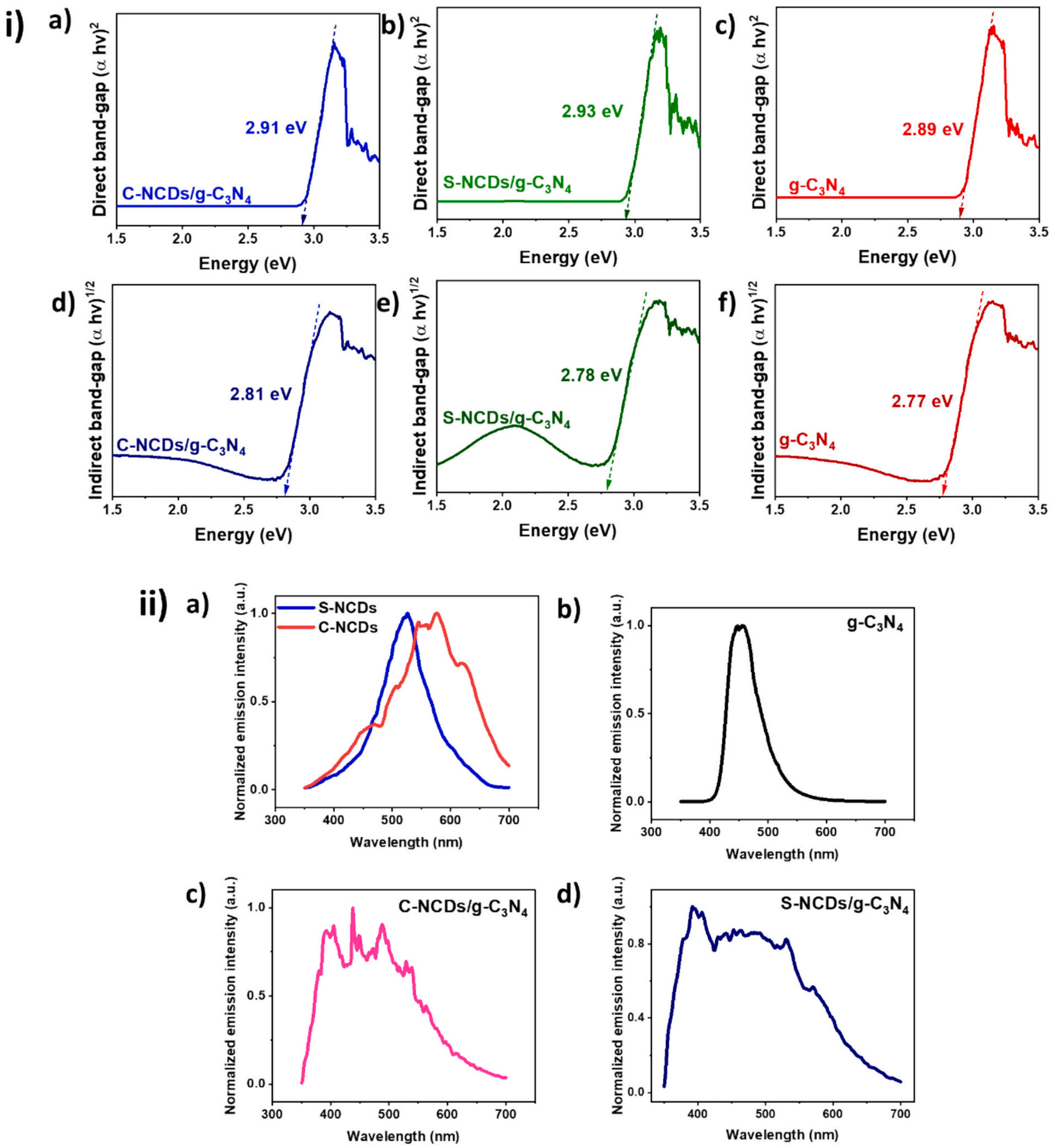

Fig. 8. **(i)** Bandgap energy determination: (direct) a) C-NCDs/g-C$_3$N$_4$, b) S-NCDs/g-C$_3$N$_4$, c) g-C$_3$N$_4$; (indirect) a) C-NCDs/g-C$_3$N$_4$, b) S-NCDs/g-C$_3$N$_4$, c) g-C$_3$N; **(ii).** Photoluminescence spectra: a) C-NCDs and S-NCDs, b) g-C$_3$N$_4$, c) C-NCDs/g-C$_3$N$_4$, d) S-NCDs/g-C$_3$N$_4$.

maximum peak emission intensity at 526 nm, indicating the presence of charge carrier recombination in an excited state; as a result, it emits a green visible light. This is a typical behavior of carbon quantum dots with uniform size distribution and surface states. Conversely, the C-NCDs also exhibit a broad band in the visible range with the maximum peak emission intensity at 575 nm but having secondary shoulder peaks around 466, 506, 546, 561, and 621 nm. Multiple peaks from C-NCDs or S-NCDs suggest a more diverse range of surface emission states. The peaks in the blue-green region (466 and 506 nm) and the redshift (621 nm) indicate a more intricate structure involving different energy levels in the emission process. The material g-C$_3$N$_4$ displayed emission peaks at around 450 nm, falling within the blue region of the spectrum, attributed to specific electronic transitions of graphitic carbon nitride, and it reflects its graphitic structure and potential defects or dopants within the lattice. For NCDs /g-C$_3$N$_4$, broad PL spectra ranging from 350 to 700 nm indicate the presence of multiple emission centers within the material. The lower end of peaks (350–450 nm) suggests a significant role in high-energy electronic transitions associated with defects or electron-hole recombination, while the 450–500 nm range indicates the existence of intermediate states within the material's structure, illustrating the presence of a potential interaction between the dopant and the carbon nitride matrix. The signals (500–700 nm region) may be attributed to lower-energy transitions, likely associated with deeper defects caused by the interactions within the doped system. This doped graphitic carbon nitride emission pattern features a wide distribution of excited states and emission centers.

3.11. Adsorption studies

The adsorption behavior of g-C_3N_4, C-NCD/g- C_3N_4, and S-NCD/g-C_3N_4 was systematically studied to remove 2,4-D from aqueous solution (Fig. 9 and Table S1). In amber bottles, the above adsorbent (1.0 mg) was poured into an aqueous solution (1.0 mL) containing 2,4-D in a concentration ranging from 2.0 to 10.0 mg/L and stirred for 12 h in a dark room to reach an optimal interaction between the adsorbent and2,4-D. Then, the mixture was centrifuged at 15,000 rpm for 5 min, and the resulting supernatant was used for the analysis. The equilibrium concentration of 2,4-D in the supernatant was determined through UV–visible spectrophotometry, measuring the concentration of 2,4-D by UV–visible spectra at 231 nm. The standard calibration curves were used to ensure analytical accuracy. The equilibrium adsorption capacity (*qe*, mol/g) was determined using the following equation: $qe = (C_o - Ce) \times V/m$. C_o = initial concentration of 2,4D (mol/L), *Ce* = equilibrium concentration (mol/L), V = solution volume (mL), and m = mass of the adsorbent material (mg). The data are plotted Ce vs. qe to obtain the equilibrium constant (qe). The models were fitted to the Langmuir equations (Eq. 4) and Freundlich equations (Eq. 5) [120,121].

$$q_e = \frac{Q_{max} K_L C_e}{1 + K_L C_e} \tag{4}$$

$$q_e = K_F C_e^{1/n} \tag{5}$$

The data are plotted Ce vs Qe to yield the equilibrium constant (q_e) by fitting the following models to the Langmuir (violet) and Freundlich (pink) equations, and the results are as follows: $q_m = 2.85 \times 10^{-5}$ mol/g for C-NCD/g-C_3N_4, 2.02×10^{-5} mol/g for S-NCD/g-C_3N_4 or 2.43×10^{-5} mol/g for g-C_3N_4. Notably, the data followed by the Langmuir and Freundlich equations indicate that the adsorption of 2,4-D is highly efficient. The Langmuir fit shows the existence of a heterogeneous catalytic surface that is capable of adsorbing 2,4-D. Notably, the data are clearly fitted into the Langmuir (violet) and Freundlich (pink) equations, indicating that the adsorption of 2,4-D by the samples is highly efficient, although the Freundlich model gives a better fit for the 2,4-D adsorption. The adsorption of 2,4-D by the samples has probably involved more complex interactions (the Freundlich model fits the behavior of a multilayer) through the different factors such as active sites, micropores, or variable surface effects [120,122].

3.12. 2,4-D degradation

The oxidation of the 2,4-D was carried out under visible/solar lights using all the above samples g-C_3N_4, C-NCDs, S-NCDs, g-C_3N_4/ C-NCDs, and S-NCDs/g-C_3N_4. 2,4-D (5.0 mg/L) was dissolved in water (100 ml), to which nano-polymer materials (30 mg/L) were added, and the whole solution was exposed under a visible light LED lamp positioned 30 cm away with an intensity of 4000 lm per square meter (lux). The concentration of 2,4-D was determined by UV–visible spectra measuring the absorption intensity at 280 nm. The same experiments were performed under sunlight for the 2,4-D oxidation by exposing the solution directly to the midday solar radiation, with an average irradiance of 50,000 lm per square meter (lux) having the spatial coordinates of 19.33, −99.18. The concentration of 2,4-D as a function of time was followed by approximately 280 nm over 3 h by UV–visible spectroscopy, measuring the concentration every 20 min by taking the solution (1.5 ml) from the reaction medium. All the experiments were carried out three times to obtain consistent results. After the reaction was finished, the nano-polymers were recovered by simple decantation. The oxidation efficiency of 2,4-D was determined according to eq. 6. The solution was kept under constant agitation in a dark room,

$$C_{\%} = 100 - \left(\frac{C_t x100}{C_t}\right) \tag{6}$$

C_t = concentration of 2,4-D at different times in the photo-catalytic process, and C_0 = initial 2,4-D concentration.

A plot of Ln [C] vs. time yielded a straight line, and the reaction is pseudo-first order in 2,4-D; the slope of the plot, which corresponds to the reaction rate constant, is directly proportional to the concentration of 2,4-D (Fig. 8) and also proportional to the catalyst concentration. The results were as follows: $k_{visible} = 4.3 \times 10^{-3}$ mM s^{-1} and $k_{solar} = 7.5 \times 10^{-3}$ mM s^{-1} for C-NCDs/g-C_3N_4; $k_{visible} = 5.4 \times 10^{-3}$ mM s^{-1} and $k_{solar} = 10.4 \times 10^{-3}$ mM s^{-1} for S-NCDs/g-C_3N_4. The results of these degradation processes under visible/solar lights are presented in Fig. 10 and Fig. S3.

The results show that S-NCDs/g-C_3N_4 oxidize 2,4-D significantly compared to other nano samples, achieving degradation of about 54.28 % (reaction rate $k = 0.0054$ mM s^{-1}) (Fig. 10a); however, under sunlight, the same material has been increased to 80.17 % with the rate constant of $k = 0.0104$ mM s^{-1} (Fig. 10b), showing that S-NCDs/g-C_3N_4 oxidize 2,4-D under sunlight exhibited a greater reaction rate with higher removal percentage. This shows the presence of heteroatoms (S, P, and N). The results obtained were compared with the different photocatalytic materials reported in the literature, as shown in Table 2.

The results demonstrate that the photocatalysts based on organic polymer have performed much better than the reported metal oxide-based photocatalysts. Moreover, the present catalytic oxidation was much smaller than that of the metal oxide-based catalysts. Fig.S3 shows the analysis of the 2,4-D degradation concentration under visible light and sunlight.

Sulfur/phosphorus-doped NCDs/g-C_3N_4 and S-NCDs/g-C_3N_4 can generate heterojunction structures, decreasing the photo-generated charge recombination (electrons and positive holes, i.e., pairs of e / h^+). The isotype heterojunction could be highly compatible structurally, and it alters the electronic structural properties, which could increase the charge separation. This means that the structural framework of NCD and g-C_3N_4 is being constructed by sp^2 hybridization; thus, combining g-C_3N_4 with CQDs would alter the electronic and structural properties.

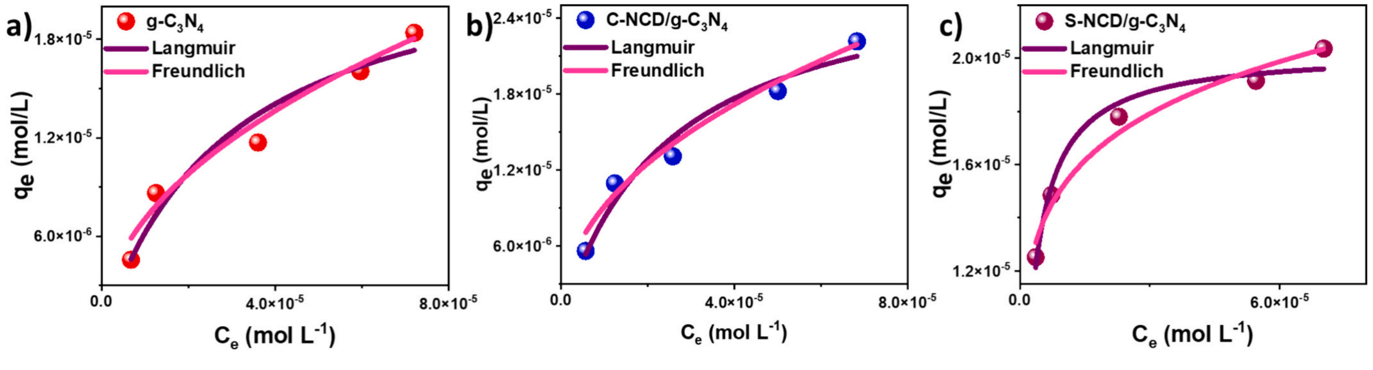

Fig. 9. Adsorption studies: a) g- C_3N_4; b) C-NCD/g- C_3N_4; and c) S-NCD/g- C_3N_4.

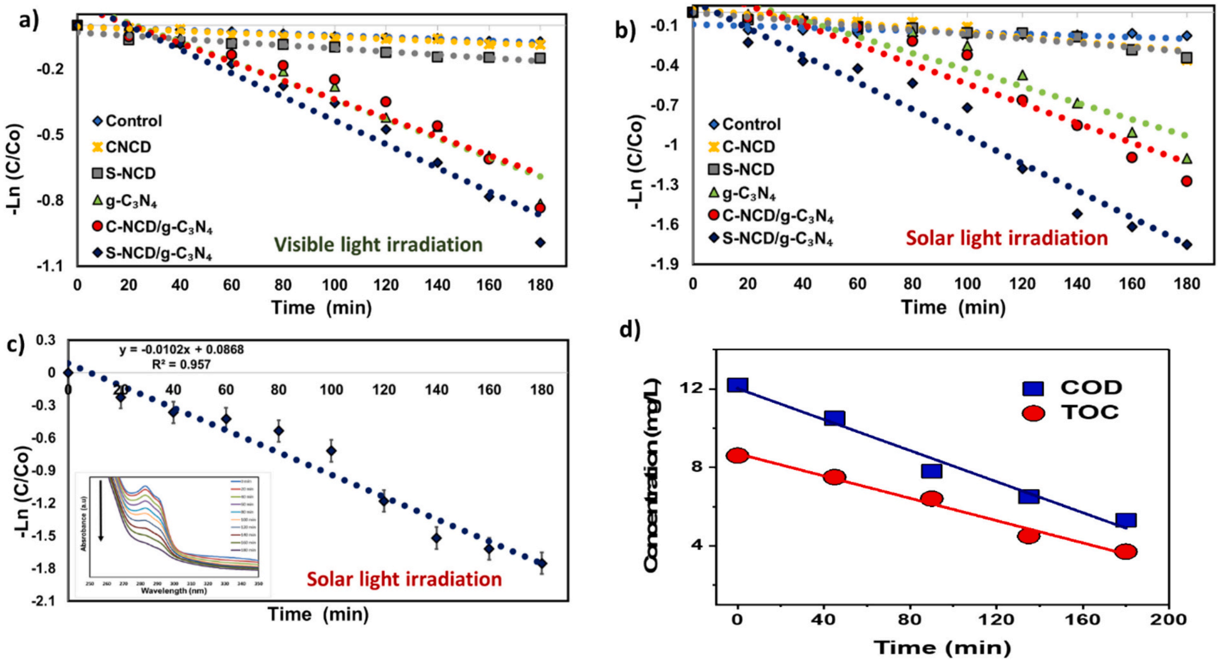

Fig. 10. Degradation of 2,4-D in the presence of g-C_3N_4, C-NCDs, S-NCDs, g-C_3N_4/ C-NCDs, and S-NCDs/g-C_3N_4 under a) visible light and b) solar light; c) degradation behavior of 2,4-D in the presence of S-NCDs/g-C_3N_4 under solar light; d) Chemical oxygen demand (COD and Total organic carbon (TOC) for the of degradation of 2,4-D using S-NCDs/g-C_3N_4 under solar light.

Table 2
Comparison of 2,4-D pesticide degradation by different catalysts.

Catalysts	[2,4-D] (ppm)	Catalysts [C, g/L]	Light	Time (min)	Remotion (%)	k (10^{-3} mM.s^{-1})	Ref.
Fe/TiO_2	40.0	1.00	UV	120	95.0	2.4	[123]
Ag/$BiFeO_3$	10.0	1.00	Visible	240	81.5	–	[124]
ZrO_2/TiO_2	58.0	0.50	UV	180	80.0	8.3	[125]
Mn/ZnO/graphene oxide	25.0	2.00	UV	120	66.2	–	[126]
S/g-C_3N_4/Ag_3VO_4	20.0	0.50	Visible	120	70.0	–	[127]
BiOBr/$MnFe_20_4$–10	20.0	1.00	Visible	80	89.3	37.5	[128]
TiO_2	11.0	0.25	UV	240	75.0	5.8	[129]
TiO_2	11.0	0.25	UV	240	45.0	2.5	[129]
C-NCDs/g-C_3N_4	50.0	0.50	Visible	180	45.70	4.3	Present work
C-NCDs/g-C_3N_4	50.0	0.50	Solar	180	66.50	7.5	
S-NCDs/g-C_3N_4	50.0	0.50	Visible	180	54.28	5.4	
S-NCDs/g-C_3N_4	50.0	0.50	Solar	180	80.17	10.4	

Moreover, with N, S, and P doping in the samples, the conductivity can be enhanced by significantly increasing the overall electron migration capability. If these atoms (S, P and N) are replaced with carbon or nitrogen in the g-C_3N_4 lattice or are located directly in the structural layers, then the photocatalytic properties certainly improve.

Chemical oxygen demand (COD) and total organic carbon (TOC) were measured during photocatalytic degradation of 2,4-D by S-NCDs/g-C_3N_4, observing a linear decrease of those parameters against time. The rate of decline was 12.2 to 5.3 mg/L for COD and 8.6 to 3.7 mg/L for TOC, showing that the TOC line decreased much faster than the COD line

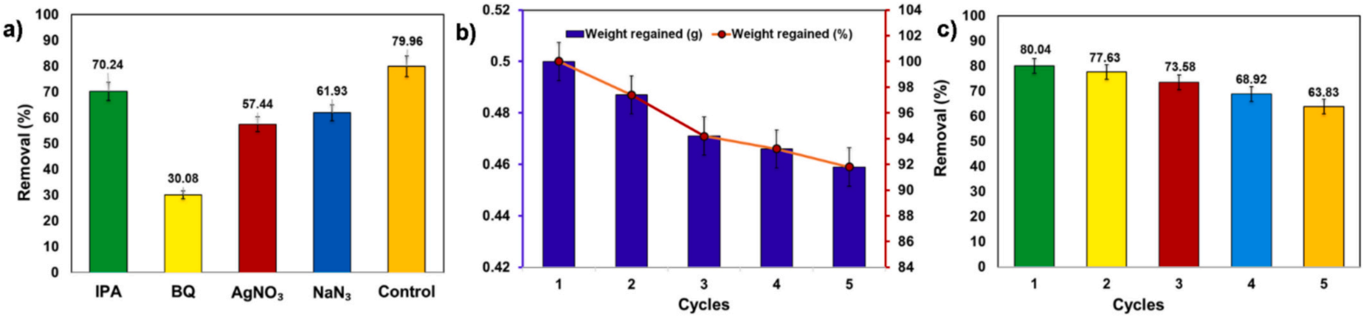

Fig. 11. a) Study of different scavengers in the photodegradation of 2,4-D, b) weight recovery in each degradation cycle and c) % removal in each catalyst reuse cycle.

because of rapid 2,4-D mineralization (Fig. 8d) by the effective catalytic properties of g-C_3N_4-doped Carbon Dots.

3.13. *Effect of radical scavenger in the degradation*

The photocatalytic degradation of 2,4-D using C-NCDs/g-C_3N_4 and S-NCDs/g-$C_3N_3N_4$ was studied under solar irradiation and evaluated scavenger effect using isopropanol (50 mM), 1,4-benzoquinone (5.0 mM), $AgNO_3$ (5.0 mM), and NaN_3 (5.0 mM) (Fig. 11a) [130–132]. In the control, where no scavenger was present, the removal efficiency was about 79.96 %. If 1,4-benzoquinone (BQ, scavenger) was present in the reaction medium, the degradation efficiency dropped sharply to 30.08 %, indicating that the scavenger captured ROS radicals, inhibiting the reaction by about 62.38 %. The addition of isopropanol (IPA), a known hydroxyl radical (•OH) scavenger, to the reaction medium results in a small decrease in the efficiency (70.24 %), with the inhibition of 12.15 %. For $AgNO_3$ addition, it is decreased to 57.44 %, with the inhibition of 28.16 %. Ag^+ ions compete by taking electrons from the ROS, reducing •O_2^- formation, and thus, they affect the photocatalytic performance of the sample. NaN_3, a known scavenger for singlet oxygen ($^1O_2$), has reduced the degradation efficiency to 61.93 %, with an inhibition of 22.54 %. (Fig. 11c). The above results show that the degradation of 2,4-D by C-NCDs/g-C_3N_4 and S-NCDs/g-$C_3N_3N_4$ can be tuned by the presence of different scavengers.

3.14. *Durability and reusability studies*

The photocatalytic stability and reusability of C-NCDs/g-C_3N_4 and S-NCDs/g-$C_3N_3N_4$ were also evaluated after considering five different consecutive degradation cycles. In the first cycle, the sample shows the removal efficiency of 80.04 %, consistent with the experimental results. If the number of cycles is increased, a gradual decrease in the efficiency of the 2,4-D oxidation is observed: for example, 2nd cycle, the removal was 77.63 %, and 3rd, 4th and 5th cycles result to 73.58 %, 68.92 %, and 63.83 %, respectively (Fig. 11c). This means, the partial decrease in the removal efficiency is commonly attributed to the partial loss of active

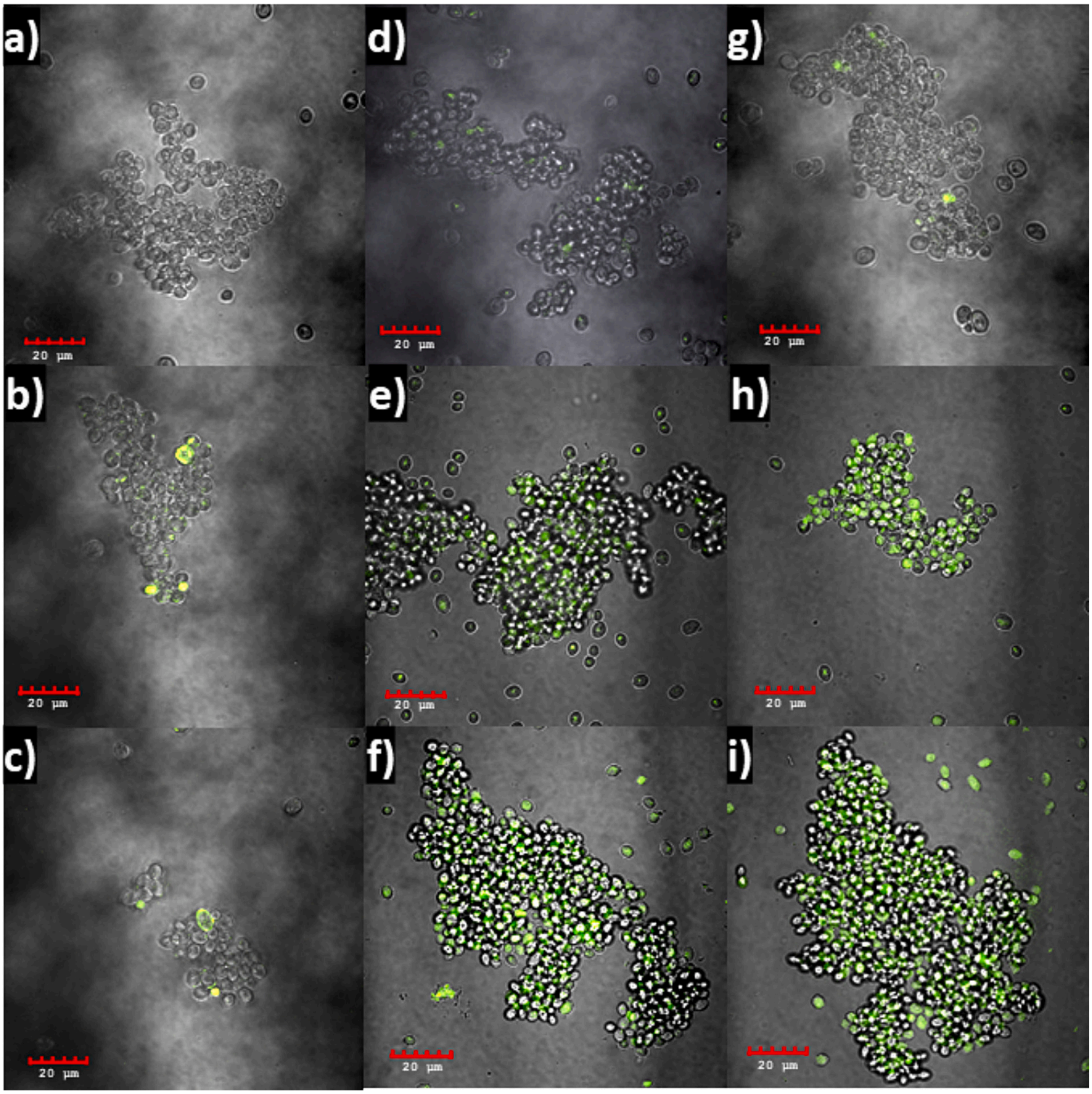

Fig. 12. Confocal microscopy images of *Saccharomyces cerevisiae*: a) Control, b) C-NCD, c) S-NCD, d) g-C_3N_4, e) C-NCD/g-C_3N_4, f) S-NCD/g-C_3N_4, g)2,4D, h) C-NCD/g-C_3N_4 + 2,4D, f) S-NCD/g-C_3N_4 + 2,4D.

sites on sample surface by its surface fouling. The recovery of the catalyst was also performed in each cycle. The initial mass of 0.5 g was fully recovered in the first cycle, but in subsequent cycles, the resulted values were: 0.487 g, 0.471 g, 0.466 g, and 0.459 g, corresponding to 97.4 %, 94.2 %, 93.2 %, and 91.8 %, respectively (Fig. 11b). It indicates that the samples are presented with high degree of physical stability and are easily recoverable. The minor losses in mass, surface active area, and surface passivation may be associated with decreased photocatalytic efficiency. This demonstrates the potential use of the sample for practical environmental applications.

3.15. Confocal bio-image of cells

Fluorescence bioimaging of *Saccharomyces cerevisiae* cells using 2,4-D in the presence and absence of C-NCD/g-C_3N_4, S-NCD/g-C_3N_4 was studied using an Olympus FV1000 instrument equipped with a diode laser (excitation 405 nm) (Fig. 12 and Fig. S4). The fluorescence intensity of the images was measured. The *Saccharomyces cerevisiae* cells were obtained commercially, purified to avoid interference from other fractions, and cultured in modified Müller-Hinton broth (MHB) with sucrose (2.0 %) as a growth factor for the inoculation. The culture was prepared in the nutrient broth medium (21 g/L in distilled water), with *Saccharomyces cerevisiae* cells (2 g/L), kept at 36 °C for 12 h. [133,134]. For control cells (100 μL), cells with other samples (C-NCD, S-NCD, g-C_3N_4, C-NCD/g- C_3N_4, S-NCD/g- C_3N_4) (200 μL 0.1 mg/mL), cells with 2,4-D (200 μL, 0.1 mM), and cells +2,4-D + nano-samples (C-NCD/g-C_3N_4 and S-NCD/g-C_3N_4) were prepared and inoculated at room temperature. The total volume was maintained at 4.0 mL for the above solution by adjusting it with MHB. The inoculated solution (30 μL) was taken and then poured onto the surface of a freshly cultured Petri dish and kept for 15 min before observing the cell performance using a confocal microscope.

The image results show that the control shows no fluorescence, while C-NCD and S-NCD exhibit dispersed fluorescence, developing the cell images. Although, for g-C_3N_4, little fluorescence image was seen, for C-NCD or S-NCD, a significant fluorescence increase was observed. For 2,4-D, we could not see an appreciable fluorescence; however, after the addition of C-NCD or S-NCD along with g-C_3N_4, a notable increase in fluorescence is observed, suggesting an interaction between C-NCD or S-NCD with the pesticide, consistent with the above adsorption studies.

3.16. DFT studies

Graphitic carbon nitride (g-C_3N_4) is known to be a semiconductor with a structure like that of graphite. From geometrical optimization, it can be observed that the materials adopt a flattened structure with distorted tridimensional geometry at the edges, given the lack of covalent C—N interaction, and for $(C_3N_4)_{46}H_{19}$, the resulting sheet had an

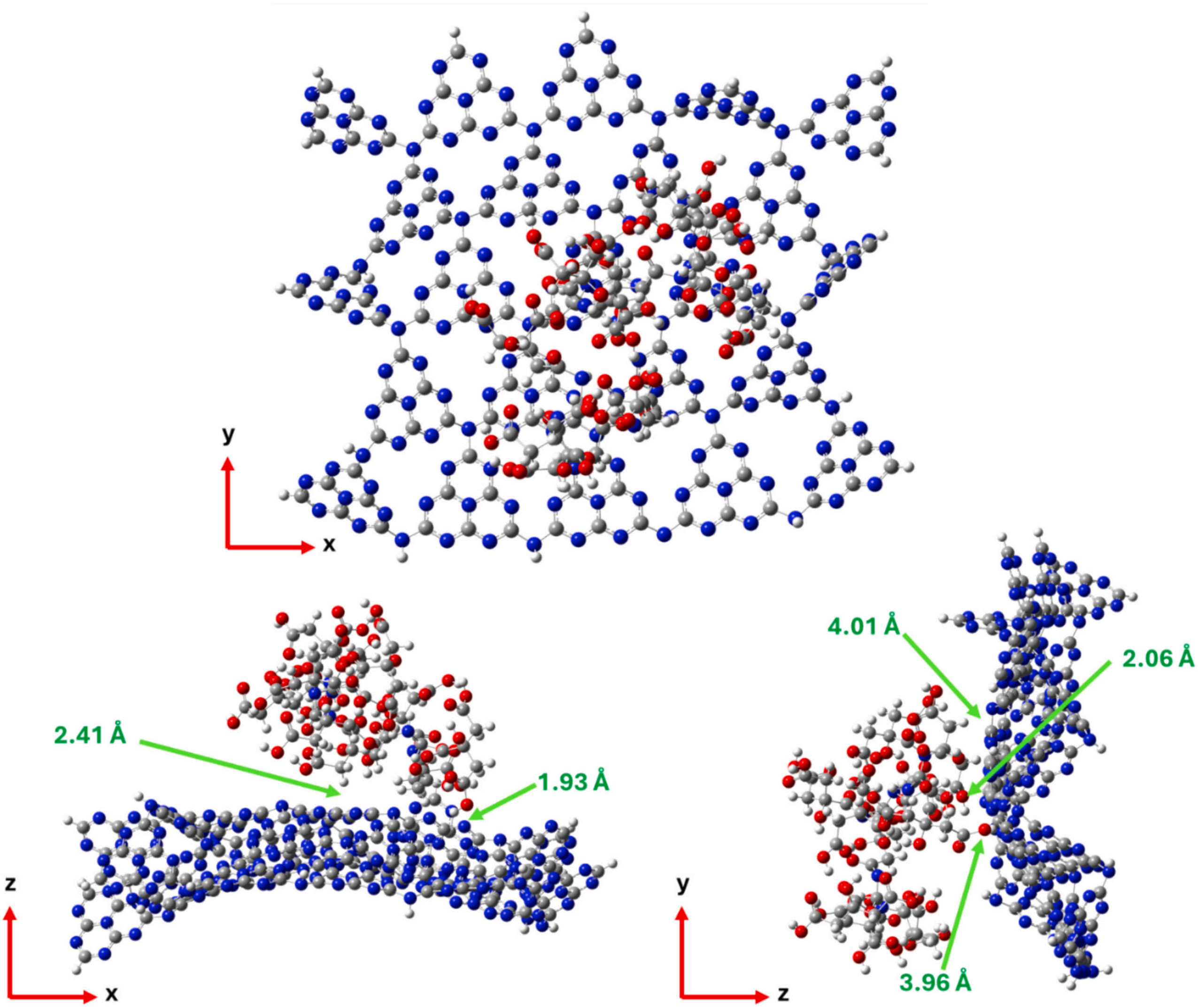

Fig. 13. Optimization geometries of NCDs/g-C_3N_4 ($C_{201}H_{93}O_{61}N_{189}$) systems through HSEh1PBE/LANL2DZ.

approximate dimension of 32 × 29 Å for a theoretical area of more than 920 $Å^2$; this value, however, is expected to be enhanced given the inherent bending of the monolayers. [135] In the case of NCDs, it can be observed that the geometry is characterized by the positioning of the highly polar carbonyl groups on the outside, whereas amide groups remain at the center of the supramolecular array [136]. The joint NCDs/$g-C_3N_4$ system revealed an electrostatic interaction where the carbon nitride matrix shows a bending toward the NCDs cluster, which highlights the effective interaction; however, no evidence of covalent bonds was found under the studied conditions (Fig. 13). Geometrical analyses revealed that the interaction takes place between $g-C_3N_4$ at the nitrogen in CN C groups and hydrogens in O—H and CH_3 from the NCDs groups. These electrostatic interactions go from strong, mostly covalent bonds (1.93–2.06 Å) to weak and mostly electrostatic bonds (2.41–4.01 Å which are within the ranges typically reported for H bonds in supramolecular arrays [137].

The addition of citric acid-urea-based NCDs modifies the band system of $g-C_3N_4$ by drifting the Fermi level toward the Conduction Band, highlighting its *n*-type semiconductor nature, where there are more available energy levels to allocate electrons (Fig. 14). For the DOS analysis, 10 S/eV units were considered to be the standard, as under this DOS, the energy gap between C_B and V_B in $g-C_3N_4$ was 2.84 eV, which is in close resemblance to that experimentally observed for graphitic carbon nitride. [138,139] This shift suggests an increase in the density of available electronic states, which enhances charge carrier mobility and reduces recombination losses, crucial for applications such as photocatalysis and optoelectronics [140]. Additionally, the presence of NCDs-induced mid-gap states could facilitate improved light absorption and broaden the activation range into the visible spectrum, further supporting the material's potential for energy conversion and environmental remediation. [141]

As can be seen in Fig. 15 and S5, NCDs/$g-C_3N_4$ is expected to be a visible light active semiconductor. From molecular orbital mapping at edge energies of conduction and valence bands; it was observed that the lower limit of C_B is located at 0.10 eV whereas the upper limit of V_B is found at −2.49 eV. The semiconductor behavior of the NCDs/$g-C_3N_4$ composite can be further understood by examining the charge transfer dynamics at the interface between the two components. The presence of carbon quantum dots (NCDs) alters the electronic structure of $g-C_3N_4$ by introducing additional energy states within the bandgap, facilitating improved charge separation and reducing recombination losses. This effect is particularly beneficial for photocatalytic applications, where efficient electron-hole pair generation and migration are crucial for enhancing catalytic performance [142]. Furthermore, the observed shift in the Fermi level toward the conduction band upon NCDs integration suggests an increase in free carrier density, reinforcing the n-type semiconductor characteristics of the composite. Such modifications not only extend the light absorption range into the visible region, as indicated by the theoretical activation wavelength cutoff of 520 nm, but also promote effective utilization of visible light, making the material a promising candidate for applications in photocatalysis, optoelectronics, and energy conversion [143].

The presence of heteroatoms, particularly sulfur and phosphorus, within the S-NCDs plays a significant role in modifying the electronic properties of the $g-C_3N_4$ matrix [36,144,145]. Sulfur atoms can introduce sub-energy levels (shallow donor levels) near the conduction band, enhancing the separation of photogenerated electron-hole pairs and facilitating electron transport. The phosphorus doping is known to introduce mid-gap states and can enhance the conductivity of the sample by narrowing the bandgap slightly. This is consistent with the Density of States (DOS), showing that the existence of these heteroatoms has increased the density of available states near the Fermi level, effectively boosting charge mobility. These are reasons why there was an improvement in the photocatalytic degradation rate of 2,4-D, because there could be a greater charge separation, reducing recombination of hole-electron pairs, which promotes the availability of reactive oxygen species for oxidation reactions.

4. Conclusion

Carbon quantum dots (NCDs) derived from fish scales are functionalized with $g-C_3N_4$ and then characterized by different analytical methods. C-NCDs/$g-C_3N_4$ and S-NCDs/$g-C_3N_4$ (~5.0–15 nm) are thermally stable and homogeneously dispersed, as shown in the SEM/TEM images. The fluorescence spectra show distinct emission profiles, implying the existence of additional electronic transitions, likely heteroatoms from the fish scales that are less pronounced for C-NCDs, consistent with the photoluminescence that the C-NCDs and S-NCDs exhibit a green visible emission. The adsorption and photocatalytic oxidation of 2,4-D by the samples was analyzed, showing that S-NCDs/g-

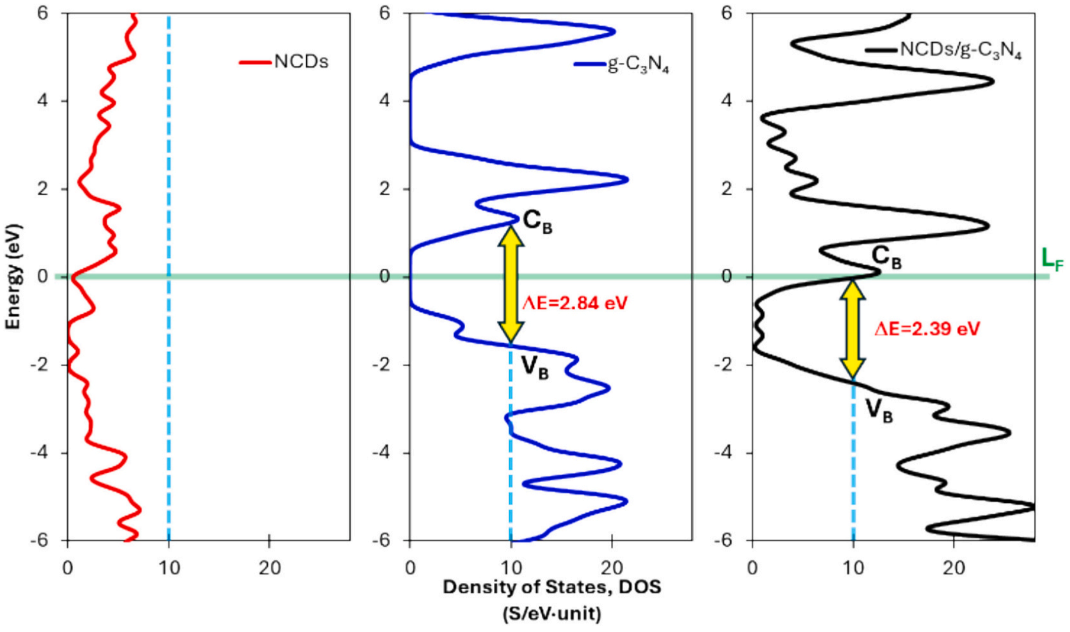

Fig. 14. Semiconductor model for tested $g-C_3N_4$-based materials.

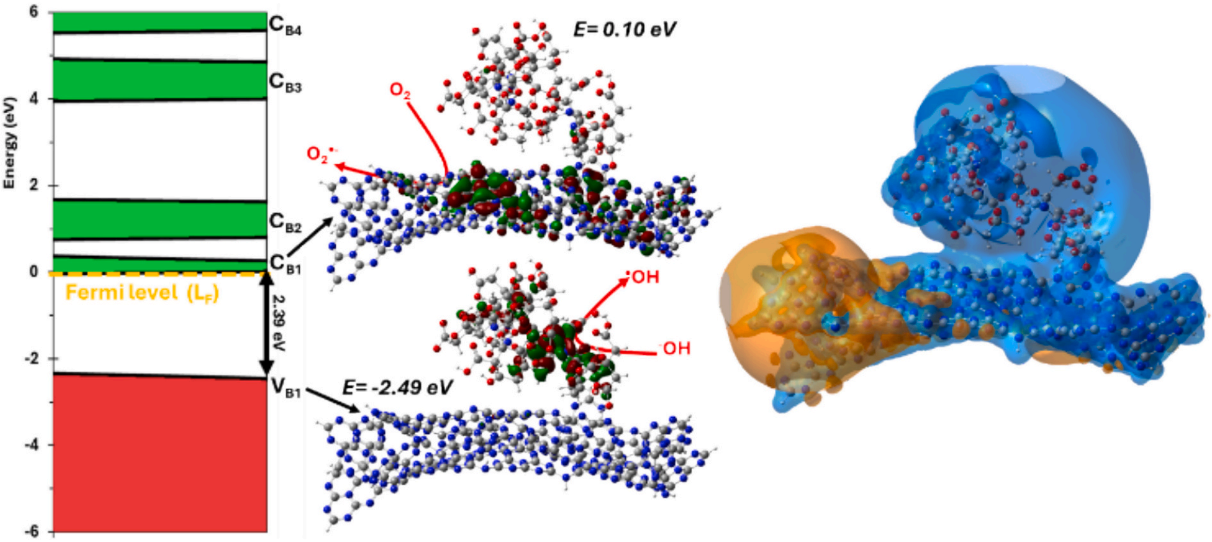

Fig. 15. Semiconductor model for NCDs/g-C_3N_4 material highlighting band system; frontier molecular orbitals at C_B and V_B and Electrostatic Potential (ESP).

C_3N_4 efficiently adsorbs the substrate ($q_m = 2.85 \times 10^{-5}$ mol/g for C-NCD/g-C_3N_4, 2.02×10^{-5} mol/g for S-NCD/g-C_3N_4 or 2.43×10^{-5} mol/g for g-C_3N_4), and there is a considerable photocatalytic oxidation, it follows first-order kinetics in the substrate as: $k_{\text{visible}} = 4.3 \times 10^{-3}$ mM s^{-1} and $k_{\text{solar}} = 7.5 \times 10^{-3}$ mM s^{-1} for C-NCDs/g-C_3N_4; $k_{\text{visible}} = 5.4 \times 10^{-3}$ mM s^{-1} and $k_{\text{solar}} = 10.4 \times 10^{-3}$ mM s^{-1} for S-NCDs/g-C_3N_4. The DFT Geometrical and electronic properties reveal that the composite maintains a non-covalent electrostatic interaction, with noticeable bending of the g-C_3N_4 structure toward the NCDs cluster. Band structure analysis indicates that the integration of NCDs modifies the electronic properties of g-C_3N_4, reinforcing its n-type semiconductor behavior. The calculated density of states (DOS) confirms an energy gap of 2.84 eV, which agrees with the experimental data. The cell image results show that there is a significant fluorescence enhancement if C-NCD and S-NCD are added to the cell culture.

CRediT authorship contribution statement

Yessenia-Scarlette García-Gutierrez: Methodology, Investigation. **Cristian-Brayan Palacios-Cabrera:** Methodology, Data curation. **Alan-Javier Santiago-Cuevas:** Validation, Methodology. **Ivan-Alejandro Reyes-Domínguez:** Visualization, Investigation, Formal analysis. **Maria-Teresa Orta-Ledesma:** Visualization, Validation. **Frank Güell:** Visualization, Methodology, Formal analysis. **Eduard Llobet:** Investigation, Data curation. **Edilso Reguera:** Data curation. **Carlos Alberto Huerta-Aguilar:** Software, Methodology. **Pandiyan Thangarasu:** Writing – review & editing, Project administration, Funding acquisition, Conceptualization.

Declaration of competing interest

The authors declare that they have no known competing financial interests or personal relationships that could have appeared to influence the work reported in this paper.

Acknowledgments

The authors gratefully acknowledge the USAI, Facultad de Quimica, for the analytical studies and the economic support for the Dirección General de Asuntos de Personal Académico (Project PAPIIT No IN202622 and IN216125) Universidad Nacional Autonoma de Mexico (UNAM). Yessenia-Scarlette thanks SECIHTI for her doctoral scholarship.

Appendix A. Supporting Information

The supporting information includes additional figures from the EDS, the map of materials, and the degradation of 2,4-D; confocal microscopy images of *Saccharomyces cerevisiae*; and adsorption values.

Data availability

Data will be made available on request.

References

[1] K. Magnoli, C.S. Carranza, M.E. Aluffi, C.E. Magnoli, C.L. Barberis, Herbicides based on 2,4-D: its behavior in agricultural environments and microbial biodegradation aspects. A review, Environ. Sci. Pollut. Res. Int. 27 (2020) 38501–38512, https://doi.org/10.1007/s11356-020-10370-6.

[2] I.M. Meftaul, K. Venkateswarlu, R. Dharmarajan, P. Annamalai, M. Megharaj, Movement and fate of 2,4-D in urban soils: a potential environmental health concern, ACS Omega 5 (2020) 13287–13295, https://doi.org/10.1021/acsomega.0c01330.

[3] A.P. Da Silva, E.R. Morais, E.C. Oliveira, N.C. Ghisi, Does exposure to environmental 2,4-dichlorophenoxyacetic acid concentrations increase mortality rate in animals? A meta-analytic review, Environ. Pollut. 303 (2022) 119179, https://doi.org/10.1016/j.envpol.2022.119179.

[4] Z.F. Li, J.X. Dong, N. Vasylieva, Y.L. Cui, D.B. Wan, X.D. Hua, J.Q. Huo, D. C. Yang, S.J. Gee, B.D. Hammock, Highly specific nanobody against herbicide 2,4-dichlorophenoxyacetic acid for monitoring of its contamination in environmental water, Sci. Total Environ. 753 (2021) 141950, https://doi.org/10.1016/j.scitotenv.2020.141950.

[5] K. Wada, N. Ohtani, Fabrication and characterization of carbon nitride fluorescent material using annealed melamine, Phys. Status Solidi B 256 (2019) 521, https://doi.org/10.1002/pssb.201800521.

[6] Y. Wang, X. Wang, M. Antonietti, Polymeric graphitic carbon nitride as a heterogeneous organocatalyst: from photochemistry to multipurpose catalysis to sustainable chemistry, Angew. Chem. Int. Ed. Eng. 51 (2012) 68–89, https://doi.org/10.1002/anie.201101182.

[7] J. Liu, H. Wang, M. Antonietti, Graphitic carbon nitride "reloaded": emerging applications beyond (photo)catalysis, Chem. Soc. Rev. 45 (2016) 2308–2326, https://doi.org/10.1039/c5cs00767d.

[8] B. Dai, J. Fang, Y. Yu, M. Sun, H. Huang, C. Lu, J. Kou, Y. Zhao, Z. Xu, Construction of infrared-light-responsive Photoinduced carriers driver for enhanced photocatalytic hydrogen evolution, Adv. Mater. 32 (2020) e1906361, https://doi.org/10.1002/adma.201906361.

[9] X.T. Wang, Y. Feng, S.O.C., Ieee computer, new method based on support vector machine in classification for hyperspectral data, in: 1st International Symposium on Computational Intelligence and DesignWuhan, Peoples R China, 2008, pp. 76–80, https://doi.org/10.1109/iscid.2008.61.

[10] H. Ou, S. Ning, P. Zhu, S. Chen, A. Han, Q. Kang, Z. Hu, J. Ye, D. Wang, Y. Li, Carbon nitride Photocatalysts with integrated oxidation and reduction atomic active centers for improved CO_2 conversion, Angew. Chem. Int. Ed. Eng. 61 (2022) e202206579, https://doi.org/10.1002/anie.202206579.

[11] M. Durandurdu, Amorphous carbon nitride (C_3N_4), J. Non-Cryst. Solids 631 (2024) 122916, https://doi.org/10.1016/j.jnoncrysol.2024.122916.

[12] Y. Zhang, D. Wen, W. Sun, J. Peng, D. Yu, X. Li, Y. Qu, J. Jiang, State-of-the-art evolution of g-C_3N_4-based photocatalytic applications: a critical review, Chin. J. Struct. Chem. 43 (2024), https://doi.org/10.1016/j.cjsc.2024.100469.

[13] P. Xia, S. Cao, B. Zhu, M. Liu, M. Shi, J. Yu, Y. Zhang, Designing a 0D/2D S-scheme heterojunction over polymeric carbon nitride for visible-light photocatalytic inactivation of Bacteria, Angew. Chem. Int. Ed. Eng. 59 (2020) 5218–5225, https://doi.org/10.1002/anie.201916012.

[14] J. Huang, D. Li, R. Li, Q. Zhang, T. Chen, H. Liu, Y. Liu, W. Lv, G. Liu, An efficient metal-free phosphorus and oxygen co-doped g-C_3N_4 photocatalyst with enhanced visible light photocatalytic activity for the degradation of fluoroquinolone antibiotics, J. Chem. Eng. 374 (2019) 242–253, https://doi.org/10.1016/j.cej.2019.05.175.

[15] J. Jiang, Z. Xiong, H. Wang, G. Liao, S. Bai, J. Zou, P. Wu, P. Zhang, X. Li, Sulfur-doped g-C_3N_4/g-C_3N_4 isotype step-scheme heterojunction for photocatalytic H_2 evolution, J. Mater. Sci. Technol. 118 (2022) 15–24, https://doi.org/10.1016/j.jmst.2021.12.018.

[16] Y. Li, M. Zhou, B. Cheng, Y. Shao, Recent advances in g-C_3N_4-based heterojunction photocatalysts, J. Mater. Sci. Technol. 56 (2020) 1–17, https://doi.org/10.1016/j.jmst.2020.04.028.

[17] J. Huang, H. Wang, H. Yu, Q. Zhang, Y. Cao, F. Peng, Oxygen doping in graphitic carbon nitride for enhanced photocatalytic hydrogen evolution, ChemSusChem 13 (2020) 5041–5049, https://doi.org/10.1002/cssc.202001317.

[18] J. Ran, T.Y. Ma, G. Gao, X.-W. Du, S.Z. Qiao, Porous P-doped graphitic carbon nitride nanosheets for synergistically enhanced visible-light photocatalytic H_2 production, Energy Environ. Sci. 8 (2015) 3708–3717, https://doi.org/10.1039/c5ee02650d.

[19] H.-B. Fang, X.-H. Zhang, J. Wu, N. Li, Y.-Z. Zheng, X. Tao, Fragmented phosphorus-doped graphitic carbon nitride nanoflakes with broad sub-bandgap absorption for highly efficient visible-light photocatalytic hydrogen evolution, Appl. Catal. B Environ. 225 (2018) 397–405, https://doi.org/10.1016/j.apcatb.2017.11.080.

[20] L. Wang, T. Yang, B. Feng, X. Xu, Y. Shen, Z. Li, J. Jiang Arramel, Constructing dual electron transfer channels to accelerate CO_2 photoreduction guided by machine learning and first-principles calculation, Chin. J. Catal. 54 (2023) 265–277, https://doi.org/10.1016/s1872-2067(23)64546-2.

[21] J. Zou, G.D. Liao, J.Z. Jiang, Z.G. Xiong, S.S. Bai, H.T. Wang, P.X. Wu, P. Zhang, X. Li, In-situ construction of sulfur-doped g-C_3N_4/defective g-C_3N_4 Iso-type step-scheme heterojunction for boosting photocatalytic H_2 evolution, Chin. J. Struct. Chem. 41 (2022) 2201025–2201033, https://doi.org/10.14102/j.cnki.0254-5861.2021-0039.

[22] F. Li, G. Zhu, J. Jiang, L. Yang, F. Deng, X. Li Arramel, A review of updated S-scheme heterojunction photocatalysts, J. Mater. Sci. Technol. 177 (2024) 142–180, https://doi.org/10.1016/j.jmst.2023.08.038.

[23] P. Xia, B. Cheng, J. Jiang, H. Tang, Localized π-conjugated structure and EPR investigation of g-C_3N_4 photocatalyst, Appl. Surf. Sci. 487 (2019) 335–342, https://doi.org/10.1016/j.apsusc.2019.05.064.

[24] T. Bharathidasan, A. Mandalam, M. Balasubramanian, P. Dhandapani, S. Sathiyanarayanan, S. Mayavan, Zinc oxide-containing porous boron-carbon-nitrogen sheets from Glycine-nitrate combustion: synthesis, self-cleaning, and sunlight-driven photocatalytic activity, ACS Appl. Mater. Interfaces 7 (2015) 18450–18459, https://doi.org/10.1021/acsami.5b04609.

[25] Y. Wang, J. Zhang, X. Wang, M. Antonietti, H. Li, Boron- and fluorine-containing mesoporous carbon nitride polymers: metal-free catalysts for cyclohexane oxidation, Angew. Chem. Int. Ed. Eng. 49 (2010) 3356–3359, https://doi.org/10.1002/anie.201000120.

[26] Q. Han, C. Hu, F. Zhao, Z. Zhang, N. Chen, L. Qu, One-step preparation of iodine-doped graphitic carbon nitride nanosheets as efficient photocatalysts for visible light water splitting, J. Mater. Chem. A 3 (2015) 4612–4619, https://doi.org/10.1039/c4ta06093h.

[27] Z.-A. Lan, G. Zhang, X. Wang, A facile synthesis of Br-modified g-C_3N_4 semiconductors for photoredox water splitting, Appl. Catal. B Environ. 192 (2016) 116–125, https://doi.org/10.1016/j.apcatb.2016.03.062.

[28] J. Zhang, J. Sun, K. Maeda, K. Domen, P. Liu, M. Antonietti, X. Fu, X. Wang, Sulfur-mediated synthesis of carbon nitride: band-gap engineering and improved functions for photocatalysis, Energy Environ. Sci. 4 (2011) 675–678, https://doi.org/10.1039/c0ee00418a.

[29] S. Guo, Z. Deng, M. Li, B. Jiang, C. Tian, Q. Pan, H. Fu, Phosphorus-doped carbon nitride tubes with a layered Micro-nanostructure for enhanced visible-light photocatalytic hydrogen evolution, Angew. Chem. Int. Ed. Eng. 55 (2016) 1830–1834, https://doi.org/10.1002/anie.201508505.

[30] J. Jiang, L. Yu, J. Peng, W. Gong, W. Sun, Advance in the modification of g-C_3N_4-based composite for photocatalytic H_2 production, Carbon Lett. 35 (2025) 417–440, https://doi.org/10.1007/s42823-024-00853-8.

[31] B. Zhu, L. Zhang, B. Cheng, J. Yu, First-principle calculation study of tri-s-triazine-based g-C_3N_4: a review, Appl. Catal. B Environ. 224 (2018) 983–999, https://doi.org/10.1016/j.apcatb.2017.11.025.

[32] Y. Li, J. Fan, J. Peng, Y. Zheng, W. Gong, J. Jiang, 2D S-doped g-C_3N_4 and V2CT x nanocomposites for ultra-sensitive electrochemical sensing uric acid, Nano Res. 18 (2025), https://doi.org/10.26599/nr.2025.94907054.

[33] H. Tan, W. Peng, T. Zhang, Y. Han, L. Yin, W. Si, J. Liang, F. Hou, Highly polymerized wine-red carbon nitride to enhance Photoelectrochemical water splitting performance of hematite, J. Phys. Chem. C 125 (2021) 13273–13282, https://doi.org/10.1021/acs.jpcc.1c02342.

[34] Y. Shan, Y. Wang, C. Shi, Z. Gan, Relaxation of excited electrons on carbon nitrides investigated by Electrochemiluminescence and photoluminescence spectra, J. Phys. Chem. C 124 (2020) 19314–19323, https://doi.org/10.1021/acs.jpcc.0c04683.

[35] P. Niu, L. Zhang, G. Liu, H.M. Cheng, Graphene-like carbon nitride Nanosheets for improved photocatalytic activities, Adv. Funct. Mater. 22 (2012) 4763–4770, https://doi.org/10.1002/adfm.201200922.

[36] Q. Tay, P. Kanhere, C.F. Ng, S. Chen, S. Chakraborty, A.C.H. Huan, T.C. Sum, R. Ahuja, Z. Chen, Defect engineered g-C_3N_4 for efficient visible light photocatalytic hydrogen production, Chem. Mater. 27 (2015) 4930–4933, https://doi.org/10.1021/acs.chemmater.5b02344.

[37] J. Qin, J. Barrio, G. Peng, J. Tzadikov, L. Abisdris, M. Volokh, M. Shalom, Direct growth of uniform carbon nitride layers with extended optical absorption towards efficient water-splitting photoanodes, Nat. Commun. 11 (2020) 4701, https://doi.org/10.1038/s41467-020-18535-0.

[38] H. Bao, L. Wang, G. Li, L. Zhou, Y. Xu, Z. Liu, M. Wu, Carrier engineering of carbon nitride boosts visible-light photocatalytic hydrogen evolution, Carbon 179 (2021) 80–88, https://doi.org/10.1016/j.carbon.2021.04.018.

[39] S.M. Ruban, K. Ramadass, G. Singh, S.N. Talapaneni, G. Kamalakar, C. R. Gadipelly, L.K. Mannepalli, Y. Sugi, A. Vinu, Organocatalysis with carbon nitrides, Sci. Technol. Adv. Mater. 24 (2023) 2188879, https://doi.org/10.1080/14686996.2023.2188879.

[40] B. Wang, M. Anpo, X. Wang, Visible light-responsive photocatalysts—from TiO_2 to carbon nitrides and boron carbon nitride, in: R. VanEldik, W. Macyk (Eds.), Mater. Renew. Sustain. Energy, 2018, pp. 49–92, https://doi.org/10.1016/bs.adioch.2018.05.008.

[41] X. Li, Q. Sun, M. Li, J. Yang, X. Chen, Y. Yang, X. Li, T. Hu, Y. Sui, X. Wu, Photocatalytic properties of nano-structured carbon nitride: a comparison with bulk graphitic carbon nitride, Int. J. Mater. Res. 109 (2018) 129–135, https://doi.org/10.3139/146.111586.

[42] Y. Zheng, L. Lin, B. Wang, X. Wang, Graphitic carbon nitride polymers toward sustainable Photoredox catalysis, Angew. Chem. Int. Ed. Eng. 54 (2015) 12868–12884, https://doi.org/10.1002/anie.201501788.

[43] S. Cao, J. Yu, G-C_3N_4-based Photocatalysts for hydrogen generation, J. Phys. Chem. Lett. 5 (2014) 2101–2107, https://doi.org/10.1021/jz500546b.

[44] J. Chu, W. Li, S. Lu, X. Rao, S. Zheng, Y. Zhang, Benzene-linked polymeric carbon nitride for enhanced photocatalytic hydrogen production, Langmuir 40 (2024) 6562–6570, https://doi.org/10.1021/acs.langmuir.4c00218.

[45] T. Gao, D. Zhao, S. Yuan, M. Zheng, X. Pu, L. Tang, Z. Lei, Energy band engineering of graphitic carbon nitride for photocatalytic hydrogen peroxide production, Carbon Energy 6 (2024), https://doi.org/10.1002/cey2.596.

[46] A. Kheradmand, A. Wainwright, L. Wang, Y. Jiang, Anchoring Iron oxides on carbon nitride nanotubes for improved photocatalytic hydrogen production, Energy Fuel 35 (2020) 868–876, https://doi.org/10.1021/acs.energyfuels.0c03901.

[47] S. Lu, H. Liu, Molecular doping on carbon nitride for efficient photocatalytic hydrogen production, Langmuir 40 (2024) 13331–13338, https://doi.org/10.1021/acs.langmuir.4c01115.

[48] X. Zhong, Y. Zhu, Y. Wang, Z. Jia, M. Jiang, Q. Sun, J. Yao, Intramolecular quaternary carbon nitride Homojunction for enhanced visible light hydrogen production, Small 20 (2024) e2402219, https://doi.org/10.1002/smll.202402219.

[49] W. Ma, D. Han, M. Zhou, H. Sun, L. Wang, X. Dong, L. Niu, Ultrathin g-C_3N_4/TiO_2 composites as photoelectrochemical elements for the real-time evaluation of global antioxidant capacity, Chem. Sci. 5 (2014) 3946–3951, https://doi.org/10.1039/c4sc00826j.

[50] J. Tian, Q. Liu, C. Ge, Z. Xing, A.M. Asiri, A.O. Al-Youbi, X. Sun, Ultrathin graphitic carbon nitride nanosheets: a low-cost, green, and highly efficient electrocatalyst toward the reduction of hydrogen peroxide and its glucose biosensing application, Nanoscale 5 (2013) 8921–8924, https://doi.org/10.1039/c3nr02031b.

[51] S. Morang, A. Bandyopadhyay, N. Borah, A. Kar, B.B. Mandal, N. Karak, Photoluminescent self-healable waterborne polyurethane/Mo and S Codoped graphitic carbon nitride nanocomposite with bioimaging and encryption capability, ACS Appl. Bio Mater. 7 (2024) 1910–1924, https://doi.org/10.1021/acsabm.3c01259.

[52] S.S. Suner, M. Sahiner, S. Demirci, E. Umut, N. Sahiner, Fluorescent graphitic carbon nitride (g-C_3N_4)-embedded hyaluronic acid microgel composites for bioimaging and Cancer-cell Targetability as viable Theragnostic, Pharmaceut 17 (2024) 160, https://doi.org/10.3390/ph17020160.

[53] Q. Zhuang, P. Guo, S. Zheng, Q. Lin, Y. Lin, Y. Wang, Y. Ni, Green synthesis of luminescent graphitic carbon nitride quantum dots from human urine and its bioimaging application, Talanta 188 (2018) 35–40, https://doi.org/10.1016/j.talanta.2018.05.060.

[54] L. Feng, F. He, G. Yang, S. Gai, Y. Dai, C. Li, P. Yang, NIR-driven graphitic-phase carbon nitride nanosheets for efficient bioimaging and photodynamic therapy, J. Mater. Chem. B 4 (2016) 8000–8008, https://doi.org/10.1039/c6tb02232d.

[55] H. Zhang, D. Zheng, Z. Cai, Z. Song, Y. Xu, R. Chen, C. Lin, L. Guo, Graphitic carbon nitride nanomaterials for multicolor light-emitting diodes and bioimaging, ACS Appl. Nano Mater. 3 (2020) 6798–6805, https://doi.org/10.1021/acsanm.0c01197.

[56] M. Xiong, Q. Rong, H.M. Meng, X.B. Zhang, Two-dimensional graphitic carbon nitride nanosheets for biosensing applications, Biosens. Bioelectron. 89 (2017) 212–223, https://doi.org/10.1016/j.bios.2016.03.043.

[57] J. Chen, D. Zhou, Z. Chen, X. Liu, Y. Xu, L. Guo, Enhanced polymeric carbon nitride Nanosheet-based fluorescence for biosensing applications, ACS Appl. Nano Mater. 6 (2023) 1441–1447, https://doi.org/10.1021/acsanm.2c05202.

[58] A. Sakthivel, A. Chandrasekaran, M. Sadasivam, P. Manickam, S. Alwarappan, Sulphur doped graphitic carbon nitride as a dual biosensing platform for the detection of Cancer biomarker CA15–3, J. Electrochem. Soc. 168 (2021) 017507, https://doi.org/10.1149/1945-7111/abd927.

[59] X. Liu, H. Zhang, Z. Song, L. Guo, F. Fu, Y. Wu, A ratiometric nanoprobe for biosensing based on green fluorescent graphitic carbon nitride nanosheets as an internal reference and quenching platform, Biosens. Bioelectron. 129 (2019) 118–123, https://doi.org/10.1016/j.bios.2019.01.032.

[60] P.Y. Liyanage, R.M. Graham, R.R. Pandey, C.C. Chusuei, K.J. Mintz, Y. Zhou, J. K. Harper, W. Wu, A.H. Wikramanayake, S. Vanni, R.M. Leblanc, Carbon nitride dots: a selective bioimaging nanomaterial, Bioconjug. Chem. 30 (2019) 111–123, https://doi.org/10.1021/acs.bioconjchem.8b00784.

[61] S. Liang, Z. Wang, Z. Zhou, G. Liang, Y. Zhang, Polymeric carbon nitride-based materials: rising stars in bioimaging, Biosens. Bioelectron. 211 (2022) 114370, https://doi.org/10.1016/j.bios.2022.114370.

[62] H. Zhang, Q. Huang, Y. Huang, F. Li, W. Zhang, C. Wei, J. Chen, P. Dai, L. Huang, Z. Huang, L. Kang, S. Hu, A. Hao, Graphitic carbon nitride nanosheets doped graphene oxide for electrochemical simultaneous determination of ascorbic acid, dopamine and uric acid, Electrochim. Acta 142 (2014) 125–131, https://doi.org/10.1016/j.electacta.2014.07.094.

[63] X. Zhang, X. Xie, H. Wang, J. Zhang, B. Pan, Y. Xie, Enhanced photoresponsive ultrathin graphitic-phase C_3N_4 nanosheets for bioimaging, J. Am. Chem. Soc. 135 (2013) 18–21, https://doi.org/10.1021/ja308249k.

[64] L. Zhao, J. Ji, Y. Shen, K. Wu, T. Zhao, H. Yang, Y. Lv, S. Liu, Y. Zhang, Exfoliation and sensitization of 2D carbon nitride for Photoelectrochemical biosensing under red light, Chemistry 25 (2019) 15680–15686, https://doi.org/10.1002/chem.201904076.

[65] Z. Zhou, Y. Zhang, Y. Shen, S. Liu, Y. Zhang, Molecular engineering of polymeric carbon nitride: advancing applications from photocatalysis to biosensing and more, Chem. Soc. Rev. 47 (2018) 2298–2321, https://doi.org/10.1039/c7cs00840f.

[66] X. Wang, K. Maeda, A. Thomas, K. Takanabe, G. Xin, J.M. Carlsson, K. Domen, M. Antonietti, A metal-free polymeric photocatalyst for hydrogen production from water under visible light, Nat. Mater. 8 (2009) 76–80, https://doi.org/10.1038/nmat2317.

[67] Z. Wu, H. Gao, S. Yan, Z. Zou, Synthesis of carbon black/carbon nitride intercalation compound composite for efficient hydrogen production, Dalton Trans. 43 (2014) 12013–12017, https://doi.org/10.1039/c4dt00256c.

[68] J. Zhang, X. Chen, K. Takanabe, K. Maeda, K. Domen, J.D. Epping, X. Fu, M. Antonietti, X. Wang, Synthesis of a carbon nitride structure for visible-light catalysis by copolymerization, Angew. Chem. Int. Ed. Eng. 49 (2010) 441–444, https://doi.org/10.1002/anie.200903886.

[69] J. Liu, W. Fu, Y. Liao, J. Fan, Q. Xiang, Recent advances in crystalline carbon nitride for photocatalysis, J. Mater. Sci. Technol. 91 (2021) 224–240, https://doi.org/10.1016/j.jmst.2021.03.017.

[70] J. Wen, J. Xie, X. Chen, X. Li, A review on g-C_3N_4 -based photocatalysts, Appl. Surf. Sci. 391 (2017) 72–123, https://doi.org/10.1016/j.apsusc.2016.07.030.

[71] W. Hou, Y. Li, S. Ouyang, H. Chen, J. Ye, X. Han, Y. Deng, Bifunctional hydroxyl group over polymeric carbon nitride to achieve photocatalytic H_2O_2 production in ethanol aqueous solution with an apparent quantum yield of 52.8% at 420 nm, Chem. Commun. (Camb.) 55 (2019) 13279–13282, https://doi.org/10.1039/c9cc07342f.

[72] W. Liu, S. Xu, S. Guan, R. Liang, M. Wei, D.G. Evans, X. Duan, Confined synthesis of carbon nitride in a layered host matrix with unprecedented solid-state quantum yield and stability, Adv. Mater. 30 (2018), https://doi.org/10.1002/adma.201704376.

[73] Y. Miyake, G. Seo, K. Matsuhashi, N. Takada, K. Kanai, Synthesis of carbon nitride oligomer as a precursor of melon with improved fluorescence quantum yield, Mater. Adv. 2 (2021) 6083–6093, https://doi.org/10.1039/d1ma00579k.

[74] M.Z. Rahman, P.C. Tapping, T.W. Kee, R. Smernik, N. Spooner, J. Moffatt, Y. Tang, K. Davey, S.Z. Qiao, A benchmark quantum yield for water Photoreduction on amorphous carbon nitride, Adv. Funct. Mater. 27 (2017), https://doi.org/10.1002/adfm.201702384.

[75] Z. Zhuo, Y. Jiao, L. Chen, H. Li, M. Dai, Z. Lin, H. Yang, F. Fu, Y. Dong, Ultra-high quantum yield ultraviolet fluorescence of graphitic carbon nitride nanosheets, Chem. Commun. (Camb.) 55 (2019) 15065–15068, https://doi.org/10.1039/c9cc07448a.

[76] J. Charoenpakdee, O. Suntijitrungruang, S. Boonchui, Investigating valley-dependent current generation due to asymmetric energy dispersion for charge-transfer from a quantum dot to single-walled carbon nanotube, Sci. Rep. 13 (2023) 3105, https://doi.org/10.1038/s41598-023-30247-1.

[77] S. Moriyama, T. Fuse, M. Suzuki, Y. Aoyagi, K. Ishibashi, Selecting single quantum dots from a bundle of single-wall carbon nanotubes using the large current flow process, Sci. Technol. Adv. Mater. 5 (2016) 613–615, https://doi.org/10.1016/j.stam.2004.02.015.

[78] J. Yang, J. Lee, J. Lee, W. Yi, Improving charge collection from colloidal quantum dot photovoltaics by single-walled carbon nanotube incorporation, ACS Appl. Mater. Interfaces 11 (2019) 33759–33769, https://doi.org/10.1021/acsami.9b07089.

[79] A. Nair, J.T. Haponiuk, S. Thomas, S. Gopi, Natural carbon-based quantum dots and their applications in drug delivery: a review, Biomed. Pharmacother. 132 (2020) 110834, https://doi.org/10.1016/j.biopha.2020.110834.

[80] W.U. Khan, L. Qin, P. Zhou, A. Alam, Z. Ge, Y. Wang, Zero thermal quenching phenomenon of green emitting carbon dots with high biocompatibility and stable multicolor biological imaging in a hot environment, ACS Appl. Mater. Interfaces 15 (2023) 45616–45625, https://doi.org/10.1021/acsami.3c09688.

[81] M.M. Caetano, A.B. Becceneri, M.V. Ferreira, R.M.N. Assuncao, R.S. da Silva, R. G. de Lima, Carbonized polymer dots: influence of the carbon nanoparticle structure on cell biocompatibility, ACS Omega 9 (2024) 38864–38877, https://doi.org/10.1021/acsomega.4c05011.

[82] P. Zhu, T. Zhang, J. Li, J. Ma, X. Ouyang, X. Zhao, M. Xu, D. Wang, Q. Xu, Near-infrared emission cu, N-doped carbon dots for human umbilical vein endothelial cell labeling and their biocompatibility in vitro, J. Appl. Toxicol. 41 (2021) 789–798, https://doi.org/10.1002/jat.4119.

[83] E. Umar, M. Ikram, J. Haider, W. Nabgan, A. Haider, M. Imran, G. Nazir, A state-of-the-art review on carbon quantum dots: prospective, advances, zebrafish biocompatibility and bioimaging in vivo and bibliometric analysis, SM&T 35 (2023) e00529, https://doi.org/10.1016/j.susmat.2022.e00529.

[84] S.Y. Lim, W. Shen, Z. Gao, Carbon quantum dots and their applications, Chem. Soc. Rev. 44 (2015) 362–381, https://doi.org/10.1039/c4cs00269e.

[85] P. Das, S. Ganguly, P.P. Maity, H.K. Srivastava, M. Bose, S. Dhara, S. Bandyopadhyay, A.K. Das, S. Banerjee, N.C. Das, Converting waste *Allium sativum* peel to nitrogen and Sulphur co-doped photoluminescence carbon dots for solar conversion, cell labeling, and photobleaching diligences: a path from discarded waste to value-added products, J. Photochem. Photobiol. B 197 (2019) 111545, https://doi.org/10.1016/j.jphotobiol.2019.111545.

[86] H. Li, S. Ye, J. Guo, H. Wang, W. Yan, J. Song, J. Qu, Biocompatible carbon dots with low-saturation-intensity and high-photobleaching-resistance for STED nanoscopy imaging of the nucleolus and tunneling nanotubes in living cells, Nano Res. 12 (2019) 3075–3084, https://doi.org/10.1007/s12274-019-2554-x.

[87] Y. Xiong, J. Schneider, C.J. Reckmeier, H. Huang, P. Kasak, A.L. Rogach, Carbonization conditions influence the emission characteristics and the stability against photobleaching of nitrogen doped carbon dots, Nanoscale 9 (2017) 11730–11738, https://doi.org/10.1039/c7nr03648e.

[88] M.X. Liu, X.B. Chen, W.Y. Liu, G.Y. Zou, Y.L. Yu, S. Chen, J.H. Wang, Dual functional full-color carbon dot-based organelle biosensor Array for visualization of lipid droplet subgroups with varying lipid composition in living cells, Anal. Chem. 95 (2023) 5087–5094, https://doi.org/10.1021/acs.analchem.2c05789.

[89] M.A.F. Nejad, A. Bigdeli, M.R. Hormozi-Nezhad, Wide color-varying visualization of sulfide with a dual emissive ratiometric fluorescence assay using carbon dots and gold nanoclusters, Microchem. J. 157 (2020) 104960, https://doi.org/10.1016/j.microc.2020.104960.

[90] Y. Han, B. Tang, L. Wang, H. Bao, Y. Lu, C. Guan, L. Zhang, M. Le, Z. Liu, M. Wu, Machine-learning-driven synthesis of carbon dots with enhanced quantum yields, ACS Nano 14 (2020) 14761–14768, https://doi.org/10.1021/acsnano.0c01899.

[91] A. Mei, Z. Xu, X. Wang, Y. Liu, J. Chen, J. Fan, Q. Shi, Photocatalytic materials modified with carbon quantum dots for the degradation of organic pollutants under visible light: a review, Environ. Res. 214 (2022) 114160, https://doi.org/10.1016/j.envres.2022.114160.

[92] X. Liu, R. Ma, L. Zhuang, B. Hu, J. Chen, X. Liu, X. Wang, Recent developments of doped g-C_3N_4 photocatalysts for the degradation of organic pollutants, Crit. Rev. Environ. Sci. Technol. 51 (2020) 751–790, https://doi.org/10.1080/10643389.2020.1734433.

[93] S. Chahal, J.R. Macairan, N. Yousefi, N. Tufenkji, R. Naccache, Green synthesis of carbon dots and their applications, RSC Adv. 11 (2021) 25354–25363, https://doi.org/10.1039/d1ra04718c.

[94] H. Guo, T. Yu, L. Zhao, J. Qian, J. Yu, Y. Zhang, Y. Teng, C. Zhu, T. Yang, W. Chen, P. Gong, C. Jiang, C. Gao, B. Yang, C. Yang, Performance study of g-C3N4/carbon black/BiOBr@Ti_3C_2/MoS_2 photocatalytic fuel cell for the synergistic degradation of different types of pollutants, Carbon Lett. 33 (2023) 847–862, https://doi.org/10.1007/s42823-023-00465-8.

[95] K. Han, G. Dong, I. Saeed, T. Dong, C. Xiao, Morphology and photocatalytic tetracycline degradation of g-C_3N_4 optimized by the coal gangue, Chin. J. Struct. Chem. 43 (2024) 100208, https://doi.org/10.1016/j.cjsc.2023.100208.

[96] X. Fu, H. Huang, G. Tang, J. Zhang, J. Sheng, H. Tang, Recent advances in g-C_3N_4-based direct Z-scheme photocatalysts for environmental and energy applications, Chin. J. Struct. Chem. 43 (2024) 100214, https://doi.org/10.1016/j.cjsc.2024.100214.

[97] N. Alhokbany, H. Althagafi, J. Ahmed, S.M. Alshehri, Synthesis and characterization of carbon dots nanoparticles for detection of ascorbic acid, Mater. Lett. 351 (2023) 134992, https://doi.org/10.1016/j.matlet.2023.134992.

[98] M. Zhang, N. Han, Y. Fei, J. Liu, L. Xing, A. Nunez-Delgado, M. Jiang, S. Liu, TiO_2/g-C_3N_4 photocatalyst for the purification of potassium butyl xanthate in mineral processing wastewater, J. Environ. Manag. 297 (2021) 113311, https://doi.org/10.1016/j.jenvman.2021.113311.

[99] S. Surender, S. Balakumar, Insight into the melamine-derived freeze-dried nanostructured g-C_3N_4 for expeditious photocatalytic degradation of dye pollutants, Diam. Relat. Mater. 128 (2022) 109269, https://doi.org/10.1016/j.diamond.2022.109269.

[100] C. Xu, X. Xiao, C. Cai, Q. Cheng, L. Zhu, J. Zhang, B. Wei, H. Wang, Insight into the differences in carbon dots prepared from fish scales using conventional hydrothermal and microwave methods, Environ. Sci. Pollut. Res. 30 (2023) 54616–54627.

[101] Z. Dai, S. Zhao, J. Lian, L. Li, D. Ding, Efficient visible-light-driven photoreduction of U(VI) by carbon dots modified porous g-C_3N_4, Sep. Purif. Technol. 298 (2022) 121590, https://doi.org/10.1016/j.seppur.2022.121590.

[102] S. Ganesan, T. Kokulnathan, S. Sumathi, A. Palaniappan, Efficient photocatalytic degradation of textile dye pollutants using thermally exfoliated graphitic carbon nitride (TE-g-C_3N_4), Sci. Rep. 14 (2024) 2284, https://doi.org/10.1038/s41598-024-52688-y.

[103] G. Chellasamy, S.R. Ankireddy, K.N. Lee, S. Govindaraju, K. Yun, Smartphone-integrated colorimetric sensor array-based reader system and fluorometric

detection of dopamine in male and female geriatric plasma by bluish-green fluorescent carbon quantum dots, Mater. Today Bio 12 (2021) 100168, https://doi.org/10.1016/j.mtbio.2021.100168.

[104] J. Liu, Z. Zhang, Z. Dong, X. Zhu, D. Gao, Z. Cheng, X. Cao, Y. Wang, Y. Liu, Metal-free CQDs introduced g-C_3N_4 nanosheets with enhanced photocatalytic reduction performance of uranium (VI), J. Radioanal. Nucl. Chem. 331 (2022) 2093–2104, https://doi.org/10.1007/s10967-022-08264-7.

[105] Y. Xin, K. Odachi, T. Shirai, Fabrication of ultra-bright carbon nano-onions *via* a one-step microwave pyrolysis of fish scale waste in seconds, Green Chem. 24 (2022) 3969–3976, https://doi.org/10.1039/d1gc04785j.

[106] J. Athinarayanan, V.S. Periasamy, A.A. Alshatwi, Simultaneous fabrication of carbon nanodots and hydroxyapatite nanoparticles from fish scale for biomedical applications, Mater. Sci. Eng. C Mater. Biol. Appl. 117 (2020) 111313, https://doi.org/10.1016/j.msec.2020.111313.

[107] Y. Ding, Z. Lin, J. Deng, Y. Liu, L. Zhang, K. Wang, S. Xu, S. Cao, Construction of carbon dots modified hollow g-C_3N_4 spheres via in situ calcination of cyanamide and glucose for highly enhanced visible light photocatalytic hydrogen evolution, Int. J. Hydrog. Energy 47 (2022) 1568–1578, https://doi.org/10.1016/j.ijhydene.2021.10.108.

[108] S. Zhang, M. Gao, Y. Zhai, J. Wen, J. Yu, T. He, Z. Kang, S. Lu, Which kind of nitrogen chemical states doped carbon dots loaded by g-C_3N_4 is the best for photocatalytic hydrogen production, J. Colloid Interface Sci. 622 (2022) 662–674, https://doi.org/10.1016/j.jcis.2022.04.165.

[109] J.S. Hiu, S.J. Phang, J. Lee, V.-L. Wong, L.-L. Tan, B-doped carbon quantum dots anchored n/n-Junctioned graphitic carbon nitride (g-C_3N_4) for CO_2 Photoreduction, in: F. Wen, J. Zhu (Eds.), Front. Energy Environ. Eng., Springer Nature Singapore, Singapore, 2024, pp. 151–157.

[110] K.S. Kim, S.Y. Choi, T.W. Kim, M.J. Kang, Recycling waste melamine-formaldehyde resin as a photocatalytic enhancer for g-C_3N_4 Photocatalysts and application in Photoelectrochemical (PEC) reactions, ACS Sustain. Chem. Eng. 12 (2024) 7083–7091, https://doi.org/10.1021/acssuschemeng.4c00748.

[111] S. Sharma, P. Chowdhury, Tunable dual photoluminescence from synthesized urea-based carbon quantum dots: a DFT based simulation on structural insights, Opt. Mater. 153 (2024) 115617, https://doi.org/10.1016/j.optmat.2024.115617.

[112] S. Šafranko, K. Janđel, M. Kovačević, A. Stanković, M. Dutour Sikirić, Š. Mandić, A. Széchenyi, L. Glavaš Obrovac, M. Leventić, I. Strelec, K. Aladić, S. Jokić, A facile synthetic approach toward obtaining N-doped carbon quantum dots from citric acid and amino acids, and their application in selective detection of Fe(III) ions, Chemosensors 11 (2023) 205, https://doi.org/10.3390/chemosensors11040205.

[113] M. Saranya Devi, T. Daniel Thangadurai, D. Nataraj, K. Naveen Kumar, Bismuth-doped carbon quantum dots as an effective fluorescent probe for metronidazole detection through inner filter effect, cytotoxicity studies, and bioimaging in zebrafish, J. Photochem. Photobiol. A Chem. 450 (2024) 115429, https://doi.org/10.1016/j.jphotochem.2023.115429.

[114] P.K. Yadav, S. Chandra, V. Kumar, D. Kumar, S.H. Hasan, Carbon quantum dots: synthesis, structure, properties, and catalytic applications for organic synthesis, Catalysts 13 (2023) 422, https://doi.org/10.3390/catal13020422.

[115] S.R. Kamali, C.-N. Chen, D.C. Agrawal, T.-H. Wei, Sulfur-doped carbon dots synthesis under microwave irradiation as turn-off fluorescent sensor for Cr(III), J. Anal. Sci. Technol. 12 (2021) 48, https://doi.org/10.1186/s40543-021-00298-y.

[116] J. Guo, Y. Lu, A.Q. Xie, G. Li, Z.B. Liang, C.F. Wang, X. Yang, S. Chen, Yellow-emissive carbon dots with high solid-state photoluminescence, Adv. Funct. Mater. 32 (2022) 2110393, https://doi.org/10.1002/adfm.202110393.

[117] B. Wang, Z. Wei, L. Sui, J. Yu, B. Zhang, X. Wang, S. Feng, H. Song, X. Yong, Y. Tian, B. Yang, S. Lu, Electron-phonon coupling-assisted universal red luminescence of o-phenylenediamine-based carbon dots, Light Sci. Appl. 11 (2022) 172, https://doi.org/10.1038/s41377-022-00865-x.

[118] W.K. Szapoczka, A.L. Truskewycz, T. Skodvin, B. Holst, P.J. Thomas, Fluorescence intensity and fluorescence lifetime measurements of various carbon dots as a function of pH, Sci. Rep. 13 (2023) 10660, https://doi.org/10.1038/s41598-023-37578-z.

[119] S. Mohandoss, S. Palanisamy, V.V. Priya, S.K. Mohan, J.-J. Shim, K. Yelithao, S. You, Y.R. Lee, Excitation-dependent multiple luminescence emission of nitrogen and sulfur co-doped carbon dots for cysteine sensing, bioimaging, and photoluminescent ink applications, Microchem. J. 167 (2021) 102032, https://doi.org/10.1016/j.microc.2021.106280.

[120] L.S. Alqarni, A.A. Alshahrani, H. Alhussain, N.Y. Elamin, M. Ismail, K.K. Taha, A. Modwi, $Bi_2Co_3O_7$@g-C_3N_4 nanocomposite for cd (II) elimination: adsorption equilibrium, kinetics and mechanistic approaches, Diam. Relat. Mater. 142 (2024), https://doi.org/10.1016/j.diamond.2024.110803.

[121] A. Saadati, S. Sheibani, Insight into the adsorption and photocatalytic properties of in-situ synthesized g-C_3N_4/SnS_2 nanocomposite, Ceram. Int. 48 (2022) 30294–30306, https://doi.org/10.1016/j.ceramint.2022.06.302.

[122] N.Y. Elamin, W. Abd El-Fattah, A. Modwi, In situ fabrication of green $CoFe_2O_4$ loaded on g-C_3N_4 nanosheets for cu (II) decontamination, Inorg. Chem. Commun. 156 (2023), https://doi.org/10.1016/j.inoche.2023.111184.

[123] U. Arellano, J.A. Wang, M. Asomoza, L.F. Chen, J. González, A. Manzo, S. Solís, V. H. Lara, Crystalline structure, surface chemistry and catalytic properties of Fe^{3+} doped TiO_2 sol–gel catalysts for photooxidation of 2,4–dichlorophenoxyacetic acid, Mater. Chem. Phys. 214 (2018) 247–259, https://doi.org/10.1016/j.matchemphys.2018.04.093.

[124] Z.H. Jaffari, S.-M. Lam, J.-C. Sin, H. Zeng, Boosting visible light photocatalytic and antibacterial performance by decoration of silver on magnetic spindle-like bismuth ferrite, Mater. Sci. Semicond. Process. 101 (2019) 103–115, https://doi.org/10.1016/j.mssp.2019.05.036.

[125] D. Guerrero-Araque, D. Ramírez-Ortega, P. Acevedo-Peña, F. Tzompantzi, H. A. Calderón, R. Gómez, Interfacial charge-transfer process across ZrO_2-TiO_2 heterojunction and its impact on photocatalytic activity, J. Photochem. Photobiol. A Chem. 335 (2017) 276–286, https://doi.org/10.1016/j.jphotochem.2016.11.030.

[126] R. Ebrahimi, M. Mohammadi, A. Maleki, A. Jafari, B. Shahmoradi, R. Rezaee, M. Safari, H. Daraei, O. Giahi, K. Yetilmezsoy, S.H. Puttaiah, Photocatalytic degradation of 2,4-Dichlorophenoxyacetic acid in aqueous solution using Mn-doped ZnO/graphene nanocomposite under LED radiation, J. Inorg. Organomet. Polym. Mater. 30 (2019) 923–934, https://doi.org/10.1007/s10904-019-01280-3.

[127] S. Joseph, S. Abraham, R.N. Priyanka, T. Abraham, A. Suresh, B. Mathew, In situ S-doped ultrathin gC_3N_4 nanosheets coupled with mixed-dimensional (3D/1D) nanostructures of silver vanadates for enhanced photocatalytic degradation of organic pollutants, New J. Chem. 43 (2019) 10618–10630, https://doi.org/10.1039/c9nj01353a.

[128] J.-C. Sin, S.-M. Lam, H. Zeng, H. Lin, H. Li, A. Kugan Kumaresan, A.R. Mohamed, J.-W. Lim, Z-scheme heterojunction nanocomposite fabricated by decorating magnetic $MnFe_2O_4$ nanoparticles on BiOBr nanosheets for enhanced visible light photocatalytic degradation of 2,4-dichlorophenoxyacetic acid and rhodamine B, Sep. Purif. Technol. 250 (2020) 117186, https://doi.org/10.1016/j.seppur.2020.117186.

[129] R. Fiorenza, A. Di Mauro, M. Cantarella, V. Privitera, G. Impellizzeri, Selective photodegradation of 2,4-D pesticide from water by molecularly imprinted TiO_2, J. Photochem. Photobiol. A Chem. 380 (2019) 111872, https://doi.org/10.1016/j.jphotochem.2019.111872.

[130] P.D. Harvey, Porphyrin-based MOFs as heterogeneous photocatalysts for the eradication of organic pollutants and toxins, J. Porphyrins Phthalocyanines 25 (2021) 583–604.

[131] J. Liu, H. Liang, Z. Xing, X. Wang, J. Bai, Synthesis of bi-$BiPO_4$-Ag_3PO_4/PAN composite nanomaterial photocatalyst with the degradation performance for rhodamine B, Mater. Sci. Semicond. Process. 185 (2025) 108918, https://doi.org/10.1016/j.mssp.2024.108918.

[132] A. Thanetchaiyakup, M. Sadek, G. Bati, Y. Xiao, X. Wang, J. Yang, Z. Liu, S. Y. Wang, H.S. Soo, Metal halide perovskites for Photocatalysis: performance and mechanistic studies, Chem. Asian J. 19 (2024) e202400787, https://doi.org/10.1002/asia.202400787.

[133] P.K. Babele, A.K. Singh, A. Srivastava, Bio-inspired silver nanoparticles impose metabolic and epigenetic toxicity to Saccharomyces cerevisiae, Front. Pharmacol. 10 (2019) 1016, https://doi.org/10.3389/fphar.2019.01016.

[134] F.S. Gustafsson, M.D. Whiteside, V. Jiranek, D.M. Durall, Development and use of a quantum dot probe to track multiple yeast strains in mixed culture, Sci. Rep. 4 (2014) 6971, https://doi.org/10.1038/srep06971.

[135] L.M. Azofra, D.R. MacFarlane, C. Sun, A DFT study of planar vs. corrugated graphene-like carbon nitride (g-C_3N_4) and its role in the catalytic performance of CO_2 conversion, Phys. Chem. Chem. Phys. 18 (2016) 18507–18514, https://doi.org/10.1039/c6cp02453j.

[136] J.D. Stachowska, A. Murphy, C. Mellor, D. Fernandez, E.N. Gibbons, M. J. Krysmann, A. Kelarakis, E. Burgaz, J. Moore, S.G. Yeates, A rich gallery of carbon dots based photoluminescent suspensions and powders derived by citric acid/urea, Sci. Rep. 11 (2021) 10554, https://doi.org/10.1038/s41598-021-89984-w.

[137] B. Dereka, Q. Yu, N.H.C. Lewis, W.B. Carpenter, J.M. Bowman, A. Tokmakoff, Crossover from hydrogen to chemical bonding, Science 371 (2021) 160–164, https://doi.org/10.1126/science.abe1951.

[138] A. Kumar, H.-P. Komsa, D. Praveen Pathak, B. Marriyappan Sivagnanam, A.S. K. Sinha, J. Karthikeyan, Origin of enhanced photocatalytic activity in direct band gap g-C_3N_4 nanoribbons with tunable electronic properties for water-splitting reaction: a first-principles study, J. Phys. Chem. C 126 (2022) 19627–19636, https://doi.org/10.1021/acs.jpcc.2c03679.

[139] R.C. Sahoo, H. Lu, D. Garg, Z. Yin, H.S.S.R. Matte, Bandgap engineered g-C_3N_4 and its graphene composites for stable photoreduction of CO_2 to methanol, Carbon 192 (2022) 101–108, https://doi.org/10.1016/j.carbon.2022.02.021.

[140] A.M.B.K. John, A.R. Chacko, C. Mohan, B. Mathew, A review on carbon quantum dot based semiconductor photocatalysts for the abatement of refractory pollutants, Chemphyschem 23 (2022) e202100873, https://doi.org/10.1002/cphc.202100873.

[141] V.C. Hoang, K. Dave, V.G. Gomes, Carbon quantum dot-based composites for energy storage and electrocatalysis: mechanism, applications and future prospects, Nano Energy 66 (2019) 104093, https://doi.org/10.1016/j.nanoen.2019.104093.

[142] Z. Zhang, T. Zheng, X. Li, J. Xu, H. Zeng, Progress of carbon quantum dots in Photocatalysis applications, Part. Syst. Charact. 33 (2016) 457–472, https://doi.org/10.1002/ppsc.201500243.

[143] M. Kouhnavard, S. Ikeda, N.A. Ludin, N.B. Ahmad Khairudin, B.V. Ghaffari, M. A. Mat-Teridi, M.A. Ibrahim, S. Sepeai, K. Sopian, A review of semiconductor

materials as sensitizers for quantum dot-sensitized solar cells, renew, Sustain. Energy Rev. 37 (2014) 397–407, https://doi.org/10.1016/j.rser.2014.05.023.

[144] A.F. Perez-Torres, D.F. Hernandez-Barreto, V. Bernal, L. Giraldo, J.C. Moreno-Pirajan, E.A. da Silva, M. Alves, J. Morais, Y. Hernandez, M.T. Cortes, M. A. Macias, Sulfur-doped g-C_3N_4 heterojunctions for efficient visible light degradation of methylene blue, ACS Omega 8 (2023) 47821–47834, https://doi.org/10.1021/acsomega.3c06320.

[145] S. Prodinger, M.A. Derewinski, Y. Wang, N.M. Washton, E.D. Walter, J. Szanyi, F. Gao, Y. Wang, C.H.F. Peden, Sub-micron cu/SSZ-13: synthesis and application as selective catalytic reduction (SCR) catalysts, Appl. Catal. B Environ. 201 (2017) 461–469, https://doi.org/10.1016/j.apcatb.2016.08.053.